arXiv:1506.08173v1 [astro-ph.EP] 26 Jun 2015

Pluto's atmosphere from stellar occultations in 2012 and 2013[1]

Dias-Oliveira, A.[1,2], Sicardy, B.[2], Lellouch, E.[2], Vieira-Martins, R.[1,3], Assafin, M.[4], Camargo, J. I. B.[1], Braga-Ribas, F.[1,5], Gomes-Júnior, A. R.[4], Benedetti-Rossi, G.[1], Colas, F.[3], Decock, A.[6,2], Doressoundiram, A.[2], Dumas, C.[7], Emilio, M.[8], Fabrega Polleri, J.[9], Gil-Hutton, R.[11,12], Gillon, M.[6], Girard, J.[7], Hau, G.[7], Ivanov, V. D.[13,14], Jehin, E.[6], Lecacheux, J.[2], Leiva, R.[15], Lopez-Sisterna, C.[11], Mancini, L.[16], Maury, A.[10], Meza, E.[2,17], Morales, N.[18], Nagy, L.[10], Opitom, C.[6], Ortiz, J. L.[18], Pollock, J.[19], Roques, F.[2], Snodgrass, C.[20], Soulier, J.F.[21], Thirouin, A.[22], Vanzi, L.[15], Widemann, T.[2], Reichart, D. E.[23], LaCluyze, A. P.[23], Haislip, J. B.[23], Ivarsen, K. M.[23], Dominik, M.[24], Jørgensen, U.[25], Skottfelt, J.[25,26]

alexoliveira@on.br

[1]Observatório Nacional/MCTI, Rua General José Cristino 77, Rio de Janeiro - RJ, 20.921-400, Brazil

[2]Observatoire de Paris/LESIA, 5 place Jules Janssen, bâtiment 10, 92195, Meudon Cédex, France

[3]IMCCE/Observatorie de Paris, 77 Avenue Denfert Rochereau, Paris, 75014, France

[4]Observatório do Valongo/UFRJ, Ladeira Pedro Antonio 43, Rio de Janeiro - RJ, 20080-090, Brazil

[5]Federal University of Technology - Paraná (UTFPR / DAFIS), Rua Sete de Setembro 3165, Curitiba - PR, 80230-901, Brazil

[6]Institut d'Astrophysique, de Géophysique et Océanographie, Université de Liège, Allée du 6 août 17, 4000 Liége, Belgium

[7]ESO, Alonso de Cordova 3107, Vitacura, 7630355 Santiago, Chile

[8]Observatório Astronômico Departamento de Geociências, Universidade Estadual de Ponta Grossa, Paraná, Brazil

[9]P.O. Box 0819-11182, Ciudad de Panama, Republica de Panama

[10]San Pedro de Atacama Celestial Explorations (S.P.A.C.E.), San Pedro de Atacama, Chile

[11]Complejo Astronómico El Leoncito (CASLEO-CONICET),Av. España 1512 sur, J5402DSP San Juan, Argentina

[12]Universidad Nacional de San Juan, Complejo Universitario "Islas Malvinas", Av. Ignacio de la Roza 590 oeste, J5402DCS - San Juan, Argentina

[13]ESO, Karl-Schwarzschild-Str. 2, 85748 Garching bei, München, Germany

[14]ESO, Alonso de Cordova 3107, Casilla 19001, Santiago 19, Chile

[15]Instituto de Astrofísica, Facultad de Física, Pontificia Universidad Católica de Chile, Av. Vicuña Mackenna 4860, Santiago 7820436, Chile

[16]Max Planck Institute for Astronomy, Königstuhl 17, D-69117, Heidelberg, Germany

[17]Facultad de Ciencias, Universidad Nacional de Ingienería, Lima, Peru

[18]Instituto de Astrofísica de Andalucía-CSIC, Apt 3004, 18080, Granada, Spain

[19]Departament of Physics and Astronomy, Appalachian State University, Boone, NC 28608, USA

[20]Planetary and Space Sciences, Department of Physical Sciences, The Open University, Milton Keynes, MK7 6AA, UK

[21]Association Des Étoiles pour Tous, 19 Rue Saint Laurent, Maisoncelles, 77320 Saint Martin du Boschet, France

[22]Lowell Observatory, 1400 W Mars Hill Rd, Flagstaff, Arizona, United States of America.

[23]Department of Physics and Astronomy, University of North Carolina - Chapel Hill, North Carolina 27599, USA

[24]SUPA, University of St Andrews, School of Physics & Astronomy, North Haugh, St Andrews, KY16 9SS, UK

[25]Niels Bohr Institute, University of Copenhagen, Juliane Maries vej 30, 2100 Copenhagen Ø, Denmark

[26]Centre for Electronic Imaging, Department of Physical Sciences, The Open University, Milton Keynes, MK7 6AA, UK

ABSTRACT

We analyze two multi-chord stellar occultations by Pluto observed on July 18th, 2012 and May 4th, 2013, and monitored respectively from five and six sites. They provide a total of fifteen light-curves, twelve of them being used for a simultaneous fit that uses a unique temperature profile, assuming a clear (no-haze) and pure N_2 atmosphere, but allowing for a possible pressure variation between the two dates. We find a solution that fits satisfactorily (i.e. within the noise level) all the twelve light-curves, providing atmospheric constraints between ∼1,190 km (pressure ∼11 μbar) and ∼1,450 km (pressure ∼0.1 μbar) from Pluto's center. Our main results are: (1) the best-fitting temperature profile shows a stratosphere with strong positive gradient between 1,190 km (at 36 K, 11 μbar) and $r = 1,215$ km (6.0 μbar), where a temperature maximum of 110 K is reached; above it is a mesosphere with negative thermal gradient of -0.2 K km^{-1} up to ∼1,390 km (0.25 μbar), where, the mesosphere connects itself to a more isothermal upper branch around 81 K; (2) the pressure shows a small (6%) but significant increase (6-σ level) between the two dates; (3) without troposphere, Pluto's radius is found to be $R_P = 1,190\pm5$ km. Allowing for a troposphere, R_P is constrained to lie between 1,168 and 1,195 km; (4) the currently measured CO abundance is too small to explain the mesospheric negative thermal gradient. Cooling by HCN is possible, but only if this species is largely saturated; Alternative explanations like zonal winds or vertical compositional variations of the atmosphere are unable to explain the observed mesospheric trend.

Subject headings: planets and satellites: atmospheres, planets and satellites: physical evolution, methods: data analysis, methods: observational, techniques: photometric

1. Introduction

Stellar occultations are a very powerful tool to discover and study, among others, tenuous atmospheres around remote bodies. Pluto's atmosphere was discovered using this technique (Brosch 1995; Elliot et al. 1989; Hubbard et al. 1988), and its spectacular two-fold expansion between 1988 and 2003 was also revealed using stellar occultations (Elliot et al. 2003; Sicardy et al. 2003). Other trans-neptunian objects were explored with this technique, and so far, none of them exhibited atmospheres at the 10 nbar pressure level (three orders of magnitude smaller than for Pluto). This includes Charon (Sicardy et al. 2006), Eris (Sicardy et al. 2011), Makemake (Ortiz et al. 2012) and Quaoar (Braga-Ribas et al. 2013).

All those bodies have sizes and surface gravities that are comparable to those of Pluto, within a factor of two. As such, the derived upper limits constrain the physical conditions necessary for the appearance and maintenance of atmospheres around a body with a given ice composition and heliocentric distance.

Here we analyze results derived from two Pluto stellar occultations (18 July 2012 and 04 May 2013) that provide signal-to-noise ratios (SNR's) that are among the best ever obtained during such events. They are furthermore combined with well-sampled multi-chord coverages, providing a good absolute radial scale for the atmosphere extension.

---

[1]Partly based on observations made with the ESO camera NACO at the Very Large Telescope (Paranal), under programme ID's 089.C-0314(C) and 291.C-5016. The prediction use observations made with the WFI camera at the 2.2 m Telescope, under programme ID's 079.A-9202(A).

We use the simplest possible model, assuming a spherically symmetric, clear (no-haze), pure N_2 atmosphere with constant temperature both horizontally and with time. Our model satisfactorily fits twelve of the selected light-curves, and provides accurate density, pressure and temperature profiles for radii between 1,190 km (11 μbar pressure level) and 1,450 km ($\sim$ 0.1 μbar) from Pluto's center, while also providing constraints on Pluto's radius.

As Pluto's atmospheric pressure is dominated by the vapor equilibrium pressure at its surface, it is very sensitive to tiny changes of temperature and the available amount of exposed ice. This induces strong seasonal effects over the plutonian year (Hansen and Paige 1996) that can be monitored and analyzed through stellar occultations (Young 2013). In that context, our data reveal a small, but significant increase of pressure between 2012 and 2013, which can be used for constraining current Pluto seasonal models, see Olkin et al. (2015) for a detailed analysis.

Our results are obtained in the context of the forthcoming flyby of the dwarf planet by the NASA *New Horizons* spacecraft in July 2015. Consequently, they can be used as a basis of comparison with the *New Horizons* findings.

2. The 2012 and 2013 Pluto stellar occultations

2.1. Predictions

From astrometric observations along Pluto's path onto the sky plane between 2008-2015, performed at the ESO's 2.2 m telescope, Assafin et al. (2010) made accurate predictions for stellar occultations involving the dwarf planet and its satellites.

In this context, the two occultations analyzed here, one on 18 July 2012 and the other on 04 May 2013, stood out as promising events, owing to the magnitudes of the candidate stars and to the presence of several potential observing sites along the shadow's path.

Follow-up astrometric observations of the stars were carried out in order to improve the predictions. These observations were made with the 1.6 m (Perkin-Elmer) and 0.6 m (Boller & Chivens) telescopes, at Pico dos dias Observatory (OPD, IAU code 874), and they are done wherever possible within our access time.

Moreover, 16 positive detections of other occultations by Pluto, that occur between 2005 and 2013, were used to improve Pluto's ephemeris offset (see Benedetti-Rossi et al. (2014) for details).

Days before the event, we carried out observations with Pluto and the occulted star present in the same field of view of our CCD's in order to minimize systematic biases like catalog errors.

2.2. Observations

The 18 July 2012 Pluto occultation was observed near zenith from five sites in South America (Fig. 1). The circumstances and technical details of the observations are provided in Table 1. The 04 May 2013 event was recorded from six sites, under similar conditions (Fig. 1), providing ten light-curves (Table 2). Various astrometric, photometric and physical parameters associated with each event are summarized in Table 3.

Fig. 2 displays the reconstructed geometries of each event, showing the Plutocentric latitudes and

altitudes probed by the primary stellar image at each site, see appendix for details. For Paranal (18 July 2012), we plot for sake of illustration the trajectories of both primary and secondary stellar images. As commented later, the contribution of the secondary image is small but not negligible compared to that of the primary image near the shadow center. Note that the primary image probes the summer (resp. winter) Pluto's hemisphere at ingress (resp. egress).

2.3. Photometry and calibration

Classical bias, dark, flat-field and sky subtraction provide the occultation light-curves displayed in Figs. 3, 4 and 5. In all cases, a reference star brighter than the target was used to correct for low-frequency transparency variations.

As expected, the best SNR light-curve was obtained at Paranal on 18 July 2012, using the NAOS-CONICA[2] (NACO) (Lenzen et al. 2003; Rousset et al. 2003) camera attached to the 8.2-m "Yepun" Very Large Telescope (VLT) of the European Southern Observatory (ESO), at a rate of 5 frames per second in H band. Moreover, this is the only data set for which we have an accurate photometric calibration, which allows us to subtract the contribution of Pluto and Charon from the occultation light-curve, see below. As such, the 18 July 2012 data provide the best constraints on Pluto's atmospheric structure. However, the 04 May 2013 light-curves have on average better SNR's than those of 18 July 2012, as well as a better spatial sampling, thus providing better constraints on the absolute vertical scale of the atmosphere.

Calibration images were taken with NACO some twenty minutes before the 2012 event. They show resolved images of Pluto, Charon and the star under excellent seeing conditions (Fig. 6). Digital coronagraphy (Assafin et al. 2008, 2009) was used to remove the star contamination from Pluto and Charon images. Classical aperture photometry finally provided the Pluto + Charon flux relative the occulted star. This allows us to estimate the residual stellar fux in the deepest part of the 18 July 2012 occultation at Paranal, with a value that varied from $2.3 \pm 0.8\%$ to $1.8 \pm 0.8\%$ of its unocculted value in the central part of the occultation (Fig. 7).

3. Modeling of Pluto's atmosphere

The general idea for modeling Pluto's atmosphere is to use an iterative procedure, combining both direct ray-tracing and inversion approaches. We first invert our best signal-to-noise ratio light-curve to retrieve Pluto's atmospheric density, pressure and temperature profiles (see Appendix and Vapillon et al. (1973)). The retrieved temperature profile is then used as a guide to generate, through direct ray-tracing, synthetic occultation light-curves that are simultaneously fitted to all the observed light-curves obtained at a given date. This pins down the location of Pluto's shadow center relative to the occultations chords for both the 2012 and 2013 events (Fig. 2). Finally, the inversion of the best light-curve is performed again and the procedure is resumed. This iterative process eventually provides the accurate geometry of each event, as well as consistent density, pressure and temperature profiles that best fit all the occultation light-curves.

Simplifying assumptions are made in our procedure (possible caveats are discussed later): (i) Pluto and its atmosphere are spherically symmetric, all quantities depend only on the radius r (defined as the distance

[2]NAOS-CONICA is Nasmyth Adaptive Optics System (NAOS) and Near-Infrared Imager and Spectrograph (CONICA)

to Pluto's body center), (*ii*) the atmosphere is transparent (no haze present), and (*iii*) it is an ideal gas in hydrostatic equilibrium, in our case, a pure molecular nitrogen N_2 atmosphere, neglecting other minor species like methane. Moreover, (*iv*) we assume that $T(r)$ is time-independent, i.e. the temperature profiles are the same in 2012 and 2013. Once $T(r)$ is derived as detailed later, the density and pressure profiles $n(r)$ and $p(r)$ are derived from the hydrostatic and ideal gas equations (Eq. A2), once a boundary condition is provided, i.e. the pressure at a given radius. (*v*) Although $T(r)$ is taken as time independent, the pressure is not. This is justified by the fact that the pressure is very sensitive to Pluto's surface temperature through the vapor pressure equilibrium equation. For instance a 1-K temperature increase at the surface results in a two-fold increase of pressure or so (Fig. 8). Thus, the pressure is a free parameter in our fits. More precisely, Eq. A2 requires a boundary condition, once $T(r)$ is fixed. So, we use as a free parameter the pressure p_r at an arbitrary radius r. We choose $r = 1,275$ km for an easier comparison with other works that provide the pressure at that level (see e.g. Olkin et al. (2015)). This level corresponds to a normalized stellar flux of ≈ 0.45 in the shadow plane. Once $p_{1,275}$ is given, the density and pressure profiles $n(r)$ and $p(r)$ are uniquely defined.

We choose the 18 July 2012 occultation light-curve obtained at VLT/NACO to perform the first inversion. We use this particular light-curve because it has the highest SNR of all (Fig. 3), and also because this is the only one for which we have a reliable measurement of the background contribution from Pluto and Charon (Fig. 7), necessary to correctly invert any occultation light-curve. The successive steps of our procedure are as follows:

(1) The inversion reveals a strong increase of temperature just above the surface (stratosphere), followed by a turning point where the temperature reaches a maximum (stratopause), then a region with a mild negative gradient (mesosphere), and finally an isothermal upper branch, see Appendix and Fig. 13. Using the prescriptions described by Eqs. A1, we adjust the coefficients $c_1, ...c_9$ controling the profile $T(r)$ in order to best fit the inverted temperature profiles (see Table 4).

(2) Keeping the profile $T(r)$ fixed in shape, we simultaneously fit seven of the light-curves obtained on 04 May 2013. The free parameters of that fit are the two coordinates defining the shadow center, the pressure $p_{1,275}$ at radius 1,275 km, and the value of r_1, the deepest point that we consider in our profile. At this stage, when r_1 is varied, all the other radii r_2, r_3 and r_4 defining $T(r)$, see Eq. A1, are changed by the same amount. In other words, the entire profile $T(r)$ is vertically displaced by this amount. Thus, r_1 eventually fixes the absolute vertical scale of the atmospheric profile. Note that r_1 is *not*, a priori, the radius of the stratobase, nor Pluto's surface radius. In practice, the choice of r_1 is made so that the stellar rays from the faint secondary image passing at r_1 have a contribution to the total flux that is negligible compared to the light-curve noise level. Thus, taking larger values of r_1 would create artificial discontinuities in the synthetic light-curve, while smaller values would require useless computation time. To find Pluto's shadow center, we separate the fit along the direction of the star motion relative to Pluto from the fit perpendicular to that direction. This is because the fit along the star motion is essentially independent of the atmospheric model, and is generally more accurate than the fit perpendicular to that direction.

Note that the 2013 light-curves have generally a better SNR than those of 2012 (excluding the VLT data set), because of a better distribution of the chords (Fig. 2). Consequently, the 2013 occultation light-curves provide a better constraint for r_1, or equivalently, for the absolute vertical scale of the atmospheric model, than those of 2012.

(3) Fixing r_1 to its value found in step (2), we turn back to the 18 July 2012 data set and simultaneously fit the five corresponding light-curves, varying Pluto's shadow center and $p_{1,275}$.

The procedure is then resumed at point (1). It is a converging process that provides consistent solutions for the shape of the profile $T(r)$, the absolute vertical scale for $T(r)$, the centers of Pluto's shadow for both events, and the two boundary conditions $p_{1,275}$ for the 18 July 2012 and 04 May 2013 events. This fitting procedure has a total of twelve free parameters: the nine coefficients $c_1, ...c_9$, the two coordinates that define Pluto's shadow center, and the pressure $p_{1,275}$.

As commented before, the 18 July 2012 NACO light-curve is the only one for which the Pluto + Charon contribution is measured (Fig. 7). So, the stellar flux was normalized between that value and the full unocculted flux before starting the fit procedure.

For the other light-curves, the inverse approach was used: the background Pluto + Charon flux was imposed by linearly adjusting the normalized, synthetic stellar flux to the actual occultation light-curve, through a least-square fit. As the residual stellar flux well inside the shadow is mainly controled by the density scale-height of the deep stratosphere (Eq. B4), this means that the structure of that region is in fact dominated by the NACO, 18 July 2012 data. The other light-curves thus mainly serve to constrain the atmospheric structure above that level (mesosphere).

4. General atmospheric structure

The best fits of our synthetic light-curves to the data are shown in Figs. 3 and 4. For each light-curve, the residuals are displayed at the bottom of the corresponding panel. They show that a unique global model satisfactorily explains all the observations, with χ^2 values per degree of freedom ($\chi^2_{\rm dof}$, see Eq. A8) close to unity, except for the 18 July 2012 NACO data (Figs. 3 and 4). In fact, due to the quality of this particular data set, the residuals are dominated by spikes associated with wave activity, as illustrated in Fig. 7. The wave activity, including the one observed in the NACO data, is discussed in details elsewhere, see French et al. (2015).

The parameters of the best atmospheric model are listed in Table 4. Note that the only parameter that differs between 18 July 2012 and 04 May 2013 is the boundary condition, i.e. the pressure $p_{1,275}$ at $r = 1,275$ km. Table 4 reveals a small (6%) but significant (6-σ level) increase of pressure, from $p_{1,275} = 2.16 \pm 0.02$ μbar in July 2012 to $p_{1,275} = 2.30 \pm 0.01$ μbar in May 2013, corresponding to a pressure increase rate of 7.5% per year.

Based on various occultation data collected, Young (2013) and Olkin et al. (2015) report a general pressure increase of some 3.5-7.5% per year between 2006 and 2013, consistent with our result above. Note that our value of $p_{1,275} = 2.30 \pm 0.01$ μbar for May 2013 differs from Olkin et al. (2015)'s result (2.70 ± 0.2 μbar) by a barely significant 0.4 ± 0.2 μbar. Part of this difference could be due to the different methods used to derive those numbers, as Olkin et al. (2015) use an isothermal fit to the upper part of the light-curves, while we use a combination of mesosphere with negative thermal gradient and an upper isothermal branch (Fig. 13).

Fig. 8 displays the density vs. radius, the temperature vs. pressure, the temperature vs. radius, and the temperature gradient of our best model. Also shown superimposed in that figure are the ingress and egress profiles retrieved from the inversions of the 18 July 2012 NACO light-curve, corresponding respectively to the summer and winter hemispheres, as far as the primary stellar image is concerned. Fig. 9 is a more detailed view of the bottom of the temperature and temperature gradient profiles, close to Pluto's surface.

The shaded areas in Fig. 8 and 9 indicate the 1-σ error envelopes caused by (i) the photometric noise

in the NACO light-curve, that mainly affects the upper parts of the profiles, and (*ii*) the uncertainty on the Pluto + Charon contribution to the total observed flux, that mainly affects the lower parts of the profiles. The methods to calculate these uncertainty domains are described in the Appendix. The temperature profiles are furthermore affected by another source of uncertainty, namely (*iii*) the a priori unknown temperature boundary condition, inherent to the nature of Eq. A2 (a first order differential equation). As examples, we show in Fig. 8 (gray lines in panels b, c and d) the profiles obtained by changing by ±5 K the nominal boundary condition ($T = 80.5$ K at $r = 1,390$ km) of the egress, inverted NACO temperature profile.

Both the photometric noise and the unknowledge of the temperature boundary condition cause an exponential divergence of the uncertainty domain for T and dT/dr as r increases, with an e-folding distance equal to the density scale height H (Eq. B3 and Fig. 8). Nevertheless, we note that *if* we have independent information on Pluto's atmosphere, e.g. from theoretical models or forthcoming observations from the *New Horizons* mission, then we can constrain our temperature at rather high altitudes. For instance, at radius $r = 1,450$ km (pressure ∼0.1 μbar), the 1-σ uncertainty on T caused by photometric noise is about ±2.5 K. Conversely, the two alternative solutions $T(r)$ given as examples in Fig. 8 (the gray lines in panel (c)), using different boundary conditions, differ from each other by 30 K at that same radius. Consequently, they can be distinguished well above the noise level if we dispose of independent constraints on the thermal properties of the atmosphere at that radius.

For instance, the warmer gray profile with strong positive temperature gradient in Fig. 8 can be discarded if we adopt current models which predict that UV heating is efficient only at much higher levels (Zhu et al. 2014). The same is true for the cooler gray temperature profile in panel (c) of Fig. 8: it shows too strong a negative gradient in the 1,400-1,450 km range, considering that atmospheric escape may cause temperatures as low as ∼ 60 K, but only much higher in the atmosphere (Ibid.).

Figs. 8 reveals three regions in our thermal profile, from bottom to top: a stratosphere with strong positive gradient that starts around 1,190 km with temperature near 36 K and pressure 11 μbar, and reaches a maximum temperature of 110 K at the stratopause (near $r = 1,215$ km, 6.0 μbar). Then follows a mesosphere with mild negative thermal gradient of -0.2 K km^{-1} up to the mesopause ($r \sim 1,390$ km, 0.25 μbar), where, it connects itself to a more isothermal upper part around 81 K. These regions are now described in detail.

5. Stratosphere

As explained in the Appendix, the residual stellar flux in the mid-part of the occultation is proportional to the local density scale-height H, which is itself related to the strong stratospheric temperature gradient (Eq. B4).

It is important to note that at closest approach to Pluto's shadow center on 18 July 2012, our model predicts that the secondary image observed at Paranal contributes by 20% to the total, primary + secondary stellar residual flux (Fig. 7). This is not negligible and explains why we have to extend our ray tracing model *below* the deepest radius obtained for the inverted temperature profiles (red and blue lines in Fig. 9). In fact, the inversion procedure assumes that there is only one (primary) stellar image contributing to the flux at any moment, while the direct ray tracing procedure does account for the presence of the two images. When the secondary image appears and disappears (at the extremities of the orange trajectory shown in Fig. 2), it reaches the radius $r_1 = 1,190.4$ km (Table 4). Its appearance and disappearance cause small discontinuities in the synthetic flux, but they are too small to be distinguished from the noise (Fig. 7).

Due to the uncertainty on the Pluto + Charon flux contribution, the deepest point of our model is determined to be at $1,190 \pm 5$ km (Fig. 9). At that point, nitrogen reaches its saturation vapor pressure (Fig. 8), and thus condenses in principle into ice, i.e. reaches Pluto's surface. In that context, we obtain a solution with a clear nitrogen atmosphere and a Pluto radius of $1,190 \pm 5$ km which consistently explains all our observations, accounting for the presence of both the primary and secondary images.

Other models are possible, though. Based a more incomplete and lower quality data set than used here, Lellouch et al. (2009) conclude that the nitrogen condensation level occurs somewhere in the range 1,187-1197 km, consistent with the present work. However, a shallow adiabatic troposphere with dry or wet nitrogen (or methane) may exist below 1,190 km. Nevertheless, there is little freedom for such tropospheric models because (*i*) they tend to create caustics in the light-curves that are not observed and (*ii*) they provide a cold methane column density that would be detected by other means. More precisely, using spectral data, Lellouch et al. (2009) find possible tropospheric solutions in a narrow region of the parameter space, with depths that cannot exceed 17 km. Similarly, combining again constraints from spectra with a preliminary analysis of the occultation data presented in this work, Lellouch et al. (2015) concluded that Pluto's radius should be between 1,180-1,188 km, some 2-8 km below the condensation radius 1,190 km derived above.

This said, we assume here that the atmosphere is haze-free, a subject of debate since the discovery of Pluto's atmosphere. Analyzing a high SNR occultation observed in 2006, Young et al. (2008) conclude that a haze-only explanation for the light-curve is extremely unlikely. In fact, the clear atmosphere model implies a temperature profile that naturally connects the maximum temperature of ∼110 K near 1,215 km to the surface at average temperature of ∼50 K (Lellouch et al. 2000, 2013), see Fig. 8 .

Other constraints come from a central flash observation during a stellar occultation in July 2007. From that event, Olkin et al. (2014) conclude that the flash is consistent with a transparent atmosphere with temperature gradient of 5 K km^{-1} at 1,196 km, fully consistent with our results (Fig. 9). Olkin et al. (2014) exclude in particular a haze-only model to explain the central flash, although combinations of thermal gradient and haze mechanism are possible. In the same vein, Gulbis et al. (2015) use a wavelength-resolved occultation on 2011 to constrain the presence of hazes in Pluto's atmosphere. Although haze models do improve the fit residuals, a clear atmosphere with a steep thermal gradient at the bottom is also consistent with the observations.

Finally, we note that the residual stellar flux exhibits a significant decrease in the bottom of the light-curve, from 2.3% to 1.8% of its unocculted value, in the central part of the occultation as observed from Paranal on 18 July 2012 (Fig. 7). This behavior was already pointed out by Sicardy et al. (2003), based on another hight SNR occultation observed in August 2002. In both cases, the residual stellar flux decreased as the primary stellar image scanned first the summer, permanently lit northern lower atmosphere, and then the winter, low insolation region (Fig. 2). This point is discussed in the last section.

6. Mesospheric negative temperature gradient

Above the stratopause ($r \sim 1,215$ km), the temperature profile exhibits a negative temperature gradient up to $r \sim 1,390$ km, with an average value of $dT/dr \sim -0.2$ K km^{-1}. In this $\sim$ 170 km radius interval, the temperature decreases by some 30 K. This mesospheric gradient is little affected by the choice of the temperature boundary condition, see Fig. 8, panel (d). While the photometric noise and the boundary condition problem induce rapidly diverging solutions for dT/dr above $\sim$ 1,400 km, the thermal gradient between $\sim$ 1,250 km and $\sim$ 1,360 km is robustly constrained around -0.2 K km^{-1}, with a typical fine-scale

scatter of ± 0.05 K km^{-1} that is dominated by Pluto's wave activity, and not by the photometric noise. In this interval, the thermal gradient remains smaller (in absolute value) than the dry adiabatic lapse rate $-g/c_p$ (Fig. 8), where g is the acceleration of gravity (Eq. A3) and $c_p = 1.04 \times 10^3$ J K^{-1} kg^{-1} is the specific heat at constant pressure for N_2. Thus, the mesosphere remains convectively stable.

Note that in principle we may choose an extreme temperature boundary condition that provides an isothermal mesosphere, i.e. a thermal profile that is much warmer than the warmer gray profile shown in panel (c) of Fig. 8. As commented earlier, however, this replaces one problem by another one, namely that the upper part of our profile is too warm, with seemingly no plausible physical explanation.

The negative mesospheric thermal gradient is further confirmed by the inversions of our best SNR light-curves obtained in July 2012 and May 2013, see Fig. 10. This eliminates random, low frequency sky-transparency variations that may have corrupted the light-curves. Moreover, such gradients have also been reported in previous, independent works. For instance Young et al. (2008) derive and discuss a $dT/dr = -0.086 \pm 0.033$ K km^{-1} gradient at $r = 1,275$ km from the 12 June 2006 occultation, while Elliot et al. (2007) give -0.17 ± 0.05 K km^{-1} for the same occultation and at the same radius. Gulbis et al. (2015) report a gradient of -0.23 ± 0.05 K km^{-1} in the 1,310-1,450 km region from the 23 June 2011 occultation, consistent with Person et al. (2013) for that event. Finally, Bosh et al. (2015) derive values of -0.17 ± 0.03 K km^{-1} and -0.24 ± 0.01 K km^{-1} around 1,280-1,300 km, for occultations observed on 09 September 2012 and 04 May 2013, respectively.

The origin of this thermal gradient is still debated. Two classes of possible explanations can be proposed: (1) the presence of cooling minor species and (2) yet unmodeled physical mechanisms. They are now examined in detail.

6.1. Possible cooling by CO or HCN

Radiative-conductive models of Pluto's atmosphere have been developed initially by Yelle and Lunine (1989); Hubbard et al. (1988); Lellouch (1994); Lellouch et al. (2015) to explain the recently-discovered gross characteristics of Pluto's atmosphere: a large lower atmosphere temperature gradient, and a warmer ($\sim$100 K) mesosphere. These studies used a simplified description of the heating/cooling properties of Pluto's atmosphere proposed by Yelle and Lunine (1989), with heating in the methane 3.3 μm band and cooling in its 7.6 μm band, both occurring in non-LTE conditions. Lellouch (1994) first suggested that additional cooling due to LTE CO emission rotational lines was important, based on an estimated abundance of CO in Pluto's atmosphere (10^{-4}-10^{-3}).

These studies were updated with the much more extensive model of Strobel et al. (1996). Notably these authors improved the treatment of solar heating in the CH_4 near-infrared bands by considering the effects of opacity and vibrational (V-V and V-T) energy transfer, and showed the need to include heating from the 2.3 μm band system in addition to the 3.3 μm bands.

As the composition of Pluto's atmosphere, as well as surface (pressure, radius) conditions, were largely unconstrained at that time, Strobel et al. (1996) explored diverse combinations of surface pressure and methane mixing ratios (including non-uniform ones), including also the effect of CO cooling. In general these models were reasonably successful at explaining large near-surface temperature gradients, though (i) fitting 10-20 K km^{-1} gradients near the surface required pushing the models to their limits, e.g. a 3.6% CH_4 mixing ratio confined to the first scale height near the surface and a 3 μbar surface (or tropopause)

pressure; (*ii*) models tended to overestimate the upper atmosphere temperature ($\sim$ 130 K instead of 100 K). A general feature of the Strobel et al. (1996) models was their prediction of a mostly isothermal atmosphere at pressures less than $\sim$ 2 μbar, though some models exhibited a moderate (0 to -0.1 K km^{-1} negative gradient at 1-2 μbar. As the direct detection of N_2 in Pluto's atmosphere is still missing, they also considered a CO-dominated atmosphere case (e.g. 97% CO + 3% CH_4). This case led, through enhanced CO cooling, to much larger negative temperature gradients in the sub-microbar region and an upper atmosphere temperature of about 55 K.

The avaibility of new, quantitative, observational constraints on the composition ($CH_4 \sim 0.5\%$, CO $\sim$ 0.05%) and near-surface structure (surface radius and pressure, tropospheric depth) of Pluto's atmosphere from near-IR observations (Lellouch et al. 2009, 2011) prompted a revival of the Strobel et al. (1996) models (Zalucha et al. 2011a,b; Zhu et al. 2014).

Model updates included new estimates of the vibrational energy transfer based on recent laboratory measurements of collisional relaxation rates (Siddles et al. 1994; Boursier et al. 2003), as well as the introduction of a scheme parameterizing the processes of eddy mixing and convection. With the updated model, Zalucha et al. (2011a) explored the effect of parameter space (CH_4 and CO mixing ratios, surface pressure and radius) allowed by the recent observations, assuming uniform vertical mixing of CH4 and CO (which was recently demonstrated to be the case for CH_4 in the first 25 km of the atmosphere, Lellouch et al. (2015)). Radiative-convective calculations were then coupled to a model generating synthetic occultation lightcurves for direct comparison to observations. The study was extended by Zalucha et al. (2011b) to include a putative troposphere.

In spite of minor changes, the Zalucha et al. (2011a,b) models confirm the essential features of the earlier Strobel et al. (1996) models. The stratopause temperature is still somewhat too high (120-125 K) near 1,215 km radius in Zalucha et al. (2011a). These models generally show only weak negative temperature gradients above this level, typically a $\sim$5 K decrease over a 300 km range for a CO mixing ratio of 5×10^{-4}, or mild $\sim$10 K decrease due to atmospheric escape (Zhu et al. 2014). This is in disagreement with the profile reported in the present study, which exhibits a typical 30 K decrease between 1,215-1,390 km and a gradient of -0.2 K km^{-1}, as discussed earlier. Rather, the profile we derive is remarkably similar to that calculated by Zalucha et al. (2011a) (their Fig. 8) for the case of 40-times enhanced CO mixing ratio (200×10^{-4}) This scenario, however, is at odds with the direct measurement of the CO abundance (Lellouch et al. 2011). This suggests that an additional cooling source is at work.

Through radiation in its intense rotational lines, HCN is the major cooling agent in Titan's upper atmosphere, where its mixing ratio is typically 2×10^{-4} at 1,100 km (Vuitton et al. 2007), and where it equilibrates the solar UV heating rates (Yelle 1991). HCN has not been detected yet in Pluto's atmosphere, but its presence is expected from coupled photochemistry in a N_2-CH_4 atmosphere. A complete re-assessment of the Pluto models is however beyond the scope of the present study. Here we only re-calculate CO cooling rates, and also examine the case of HCN cooling. Photochemical models predictions lead to rather diverse mixing ratios of HCN (10^{-8}-10^{-3} of N_2 (Summers et al. 1997; Lara et al. 1997; Krasnopolsky and Cruikshank 1999), where the difference largely seems to come from the fact that the more "optimistic" models have not accounted for the fact that under cold ($<$ 100 K) temperatures, atmospheric condensation of HCN should occur. Here, we nominally consider cases in which the HCN abundance is limited by the saturation law (Fray and Schmitt 2009), but we also run a case with uniformely mixed HCN, as supersaturation may be possible in a clear, tenuous atmosphere as Pluto's. Cooling rates at radius r are calculated from the following

equation (e.g. for CO):

$$R_{CO}(r) = 4\pi N_{CO}(r) \int B_\nu(T(r)) k_\nu E_2(\tau_\nu) d\nu, \quad (1)$$

where N_{CO} is the local CO number density, T is temperature, k_ν and τ_ν are the absorption coefficients and zenithal opacity at frequency ν, and $E_2(\tau)$ is the second exponential integral. The integral runs over the entire mm/submm range (0-200 cm^{-1}), and unlike in Strobel et al. (1996), we include all isotopic variants of CO (HCN). Moreover, absorption coefficients are calculated using a Voigt profile, instead of the Doppler approximation. Both aspects lead to a minor but non-negligible increase in the cooling rate at low altitudes. Calculations of the cooling rates are performed for the thermal profile inferred in this work.

Results are shown in Fig. 11 for a series of assumed CO and HCN profiles. The CO mixing ratio $q_{\rm CO} = 5 \times 10^{-4}$ curves show the "nominal" CO cooling. Although Zalucha et al. (2011a,b) do not show their cooling rates, our calculation for CO can be compared to Figure 5a of Zhu et al. (2014), showing reasonable agreement. Increasing the $q_{\rm CO}$ by a factor of 40 leads to an increase of the cooling rate, although in much lower proportion due to opacity effects.

Other curves in Fig. 11 show the cooling due to HCN for different assumed HCN mixing ratios in the non-saturated part of the atmosphere. For the temperature profile derived in this work, the lower temperatures above 1270 km radius, severely restrict the amount of gaseous HCN if saturation of HCN is accounted for. In fact, HCN appears to be saturated everywhere in the atmosphere, except possibly over the 1210-1270 km range, where the condensation law allows 10^{-7}-10^{-6} HCN mixing ratios. There, the HCN cooling rate may slightly exceed the nominal CO cooling rate (pink vs. red curves in the left panel of Fig. 11). However, for the HCN cooling rates to approach the "enhanced" CO cooling rates necessary to explain our negative mesospheric temperature gradient (i.e. those for $q_{\rm CO} = 200 \times 10^{-4}$, as considered by Zalucha et al. (2011a)), one must assume that HCN is not limited by saturation. Specifically, the blue curve in Fig. 11 shows that a uniform HCN mixing ratio of $\sim 5 \times 10^{-5}$ is required.

Although a full re-assessment of the radiative-models should be undertaken at this point, we conclude from this exercise that there is no obvious "culprit" for a -0.2 K km^{-1} temperature gradient above the radius $\sim$ 1220 km. According to the calculations of Zalucha et al. (2011a), CO in amounts consistent with the direct observations of Lellouch et al. (2011) provide unsufficient cooling. We show here that HCN could be an alternative efficient cooling agent, but only if its mixing ration vastly exceeds expectations from the condensation law. Direct measurements/upper limits of HCN from ALMA and perhaps from New Horizons UV spectrometer (ALICE) will bring new light on this issue.

6.2. Alternative explanations

Coming back a step, the primary result derived from a stellar occultation light-curve is the refractivity profile $\nu(r)$, from which a density profile $n(r) = \nu(r)/K$ is obtained, assuming a given gas composition (Eq. A4).

A first idea is to envisage that hazes are present in the mesosphere. Those hazes would absorb part of the stellar flux, in such a way that a basically isothermal mesosphere is thought to host a negative thermal gradient just because of the clear-atmosphere assumption. To test that hypothesis, we have generated synthetic light-curves, forcing the mesosphere to be isothermal at $T_{\rm iso} = 95.5$ K above the stratopause (we have also tested other values of $T_{\rm iso}$ between 85 and 110 K, with the same conclusions). Fig. 3 shows the resulting residuals for the NACO 18 July 2012 light-curve (labelled "iso." in that figure). They depart from

zero well above the noise level, and we can rule out photometric fluctuations caused by absorbing haze layers, since the residuals have both positive and negative values.

This said, two assumptions may be wrong in Eq. A2: (1) the atmosphere may be not composed of pure nitrogen N_2, so that the nitrogen molecular mass μ must be replaced by a new value μ', and (2) hypothetical zonal winds may create a centrifugal acceleration, so that the acceleration of gravity g must be replaced by a term g' that includes supplementary terms.

In fact, we can use Eq. A2 in a reversed way. More precisely, the refractivity profile $\nu(r)$ is actually an *imposed* observable (since it is directly derived from the occultation light-curve), while we may use a *prescribed* temperature profile $T'(r)$, for instance taken from a theoretical model. With this approach in mind, Eq. A2 can be re-written:

$$\frac{\mu' g'}{\mu g} = -\frac{kT'}{\mu g}\frac{d\log(\nu T')}{dr}. \tag{2}$$

To obtain this equation, we have used $\nu(r) = K \cdot n(r)$, where K is the molecular refractivity (Eq. A4). We assume here that the atmospheric composition varies slowly with radius (i.e. K suffers small variations over one scale-height), so that we neglect dK/dr, and finally provide $d[\log(\nu)]/dr \sim d[\log(n)]/dr$.

Thus, the ratio $\mu' g'/\mu g$ is the factor by which the molecular mass and/or the acceleration of gravity g must be multiplied in order to retrieve a prescribed temperature profile $T'(r)$, given an observed occultation light-curve.

In Fig. 12, we consider an example where the prescribed temperature profile $T'(r)$ exhibits a decrease of only 10 K between the stratopause and the mesopause. This is typical of what can be obtained by the combined effects of CO cooling (Zalucha et al. 2011a) and/or a atmospheric escape (Zhu et al. 2014). The right panel of Fig. 12 shows the resulting profile for $\mu' g'/\mu g$, restricting ourselves to the mesospheric region.

We first assume here that the atmosphere is composed of pure nitrogen, so that $\mu' = \mu$, and the ratio $\mu' g'/\mu g = g'/g$ is only caused by variations of g'. In the presence of a zonal wind with velocity v, the centrifugal acceleration provides $g' = g - v^2/r$, and from $g = GM/r^2$, a zonal wind of:

$$v = \sqrt{\frac{GM}{r}} \cdot \sqrt{1 - \frac{g'}{g}} \sim 840\sqrt{1 - \frac{g'}{g}} \text{ m s}^{-1}, \tag{3}$$

where we have used the value of GM in Table 3 and $r \sim 1,250$ km. With the example above, the factor g'/g' reaches a minimum value of about 0.95, yielding $v \sim 190$ m s^{-1}. This is close to supersonic, as the speed of sound for nitrogen N_2 at 100 K is about 200 m s^{-1}. In fact, current General Circulation Models (GCM's) for Pluto predict zonal winds of less than 10 m s^{-1} at the altitudes considered here (Vangvichith 2013; Zalucha and Michaels 2013). Moreover, we see that above $r \sim 1,300$ km, the ratio g'/g becomes larger than unity with the example considered here, which is impossible from Eq. 3. Other prescribed profiles $T'(r)$ could be imagined to avoid this problem by displacing the $\mu' g'/\mu g$ profile to the left in Fig. 12 (providing smaller values of g'/g), but this would imply even more unrealistic, high zonal winds.

Considering that $g'/g \sim 1$ from the discussion above, the $\mu' g'/\mu g$ profile would represent variations of molecular of the atmospheric molecular weight, μ'/μ. In the example of Fig. 12, the molecular weight of the atmosphere has to be inferior to that of molecular nitrogen, μ, to mimic the effect of a negative temperature gradient. This could be caused by the presence of a lighter gas, for instance neon, which has a molecular weight $\mu_{\rm Ne} \sim 0.72\mu$. That species has a relatively large solar abundance ($N_e/N \sim 1.5$) and is not condensed at Pluto's atmospheres temperatures. The minimum value $\mu'/\mu = 0.95$ near 1,230 km (Fig. 12) would then require a local neon abundance of about 82%. However, and as before, the ratio μ'/μ would be larger than

unity above 1,300 km, requiring that another, heavier, gas (e.g. argon) takes over above 1,300 km and drives the molecular mass upwards. Such model is clearly unrealistic though, because mass separation would result in a depletion, not enrichment, of the heavier species in the upper atmosphere.

7. Upper atmosphere

Above $r \sim 1,400$ km, the results of Fig. 8 shows that a change of thermal gradient may occur, with a more isothermal upper branch just above the mesosphere. However, the lack of independent constraints on the temperature at that level prevents an unambiguous choice for a particular solution for $T(r)$. In addition, the rapidly increasing contribution of the noise makes impossible any estimation of the thermal gradient above 1,450 km (Fig. 8, panel (d)). This said, the lack of obvious mechanisms to drastically warm up or cool down the atmosphere just above 1,400 km suggests (but by no means proves) an isothermal branch between 1,400 and 1,450 km. Under this hypothesis, we estimate a 1-σ uncertainty domain of 81 ± 6 K for the temperature of this isothermal branch. (This interval corresponds to an increase of $\Delta\chi^2 = +1$ of the χ^2 function with respect to the best, minimum value $\chi^2_{\rm min}$).

8. Discussion and conclusions

We have analyzed among the best light-curves ever obtained during stellar occultations by Pluto. Combination of well-sampled occultation chords (Fig. 2) and high SNR data (Figs. 3,4) have allowed us to constrain the density, temperature and thermal gradient profiles of Pluto's atmosphere between radii $r \sim 1,190$ km (pressure $p \sim 11$ μbar) and $r \sim 1,450$ km (pressure $p \sim 0.1$ μbar). Our main results are listed below.

Global Pluto's atmospheric model. We find that a unique thermal model can fit satisfactorily twelve light-curves observed in 2012 and 2013 (Figs. 3 and 4), assuming a spherically symmetric and clear (no haze) atmoshere. The parameters defining our best model are listed in Table 4 (see also Fig. 13), and the various resulting profiles (density, temperature and thermal gradient) are displayed in Figs. 8, 9 and 10. The absolute vertical scale of our global model has an internal accuracy of about ± 1 km (Table 4). However, this error is amplified to ± 5 km at the bottom of the profiles (Fig. 9), because of the uncertainty on the residual stellar flux (Fig. 7) in the central part of the occultation observed by NACO on 18 July 2012.

We quantify in this work the propagation of the photometric noise into the density, temperature and thermal gradient profiles (Eqs. B3 and Fig. 8). The key parameter that governs the noise propagation is the radius r_0 in the amosphere at which the stellar drop caused by differential refraction is equal to the flux standard deviation. The radius r_0 can be estimated from Eq. B2, which includes all the quantities at work in a stellar occultation: photometric noise, molecular refractivity, atmospheric scale-height and radius, and distance to the body. For the NACO light-curve, we find $r_0 = 1,565$ km, corresponding to a pressure level of about 14 nbar.

Although a satisfactory fit to all the data used here is provided by a unique model, there are two slight, but significant departures from this global model. They are now discussed in turn.

Pressure increase between 2012 and 2013. In the frame of our model (i.e. assuming a constant temperature profile), we detect a significant 6% pressure increase (at the 6-σ level) during the ~9.5 months separating the two events under study. This means that Pluto's atmosphere was still expanding at that time, confirming the work of Olkin et al. (2015), which compiles and analyzes pressure measurements between 1988 and 2013.

Ingress/egress asymmetry of lower temperature profiles. Fig. 7 shows that the stellar flux decreased from 2.3% to 1.8% of its unocculted value during the central part of the 18 July 2012 occultation, as observed by NACO from Paranal. This corresponds to the primary stellar image first scanning the summer, permanently lit Pluto northern hemisphere, and then the winter low insolation southern hemisphere (Fig. 2). This confirms a similar trend pointed out by Sicardy et al. (2003) during another high SNR stellar occultation recorded in August 2002. These authors interpreted this result as a surface boundary layer effect, where the lowermost scale-height adjusts itself to the surface temperature variegations, which might explain the behavior displayed in Fig. 9.

Another interpretation of this trend is the gradual entrance of the primary stellar image into an absorbing haze layer near Pluto's evening limb, a hypothesis that can be tested during the *New Horizons* flyby in July 2015.

Pluto's radius and density. The extrapolation of our temperature profiles to the nitrogen saturation line implies that nitrogen may condense at a Pluto's radius of $R_P = 1,190 \pm 5$ km. However, the few kilometers above Pluto's surface remain *"terra incognita"* as far as stellar occultations are concerned. In particular, the temperature gradients shown in Fig. 9 may deviate from the simple extrapolation used here, especially if haze layers affect the retrieved temperature profiles. Although difficult to envisage because of the strong caustics that they cause, a troposphere below $1,190 \pm 5$ km cannot be excluded. Combining high-resolution spectroscopic observations of gaseous methane, combined with constraints from an occultation observed in 2002, Lellouch et al. (2009) conclude that the troposphere depth cannot exceed about 17 km. Consequently (and assuming that the temperature of the deep atmosphere did not change significantly since 2002), our observations constrain Pluto's radius to lie in the range 1,168-1,195 km. More recently, combining constraints from spectra and a preliminary analysis of the occultation data presented in this work, Lellouch et al. (2015) concluded that Pluto should have a radius between 1,180-1,188 km, some 2-8 km below the condensation radius of 1,190 km that we derive above.

From a Pluto's mass of $M_P = 1.304 \pm 0.006 \times 10^{22}$ kg (Tholen et al. 2008), we derive a density $\rho_P = (1.802 \pm 0.007)(R_P/1,200 \text{ km})^{-3}$ g cm^{-3}. Our estimation $R_P = 1,190 \pm 5$ km thus implies $\rho_P = 1.85 \pm 0.02$ g cm^{-3} in the absence of troposphere, and a range $\rho_P = 1.83 - 1.95$ g cm^{-3} if a troposphere is allowed. This is larger, but not by much, than Charon's density, $\rho_C = 1.63 \pm 0.05$ g cm^{-3} (Ibid.).

The mesospheric negative thermal gradient. Pluto's stratopause occurs near 1,215 km (pressure $p = 6.0$ μbar), with a maximum temperature of 110 ± 1 K, where the error bar applies to the best inverted profile (NACO 18 July 2012), and stems from the uncertainty on the Pluto + Charon flux contribution (Fig. 8).

Above the stratopause, and up to about 1,390 km, our best 2012 and 2013 occultation light-curves yield inverted temperature profiles with a negative thermal gradient close to -0.2 K km^{-1} which amounts to a total decrease of 30 K for the temperature between 1,215 and 1,390 km (Figs. 8,10)

Explaining this negative gradient by CO cooling requires a mixing ratio (200×10^{-4}) that is too high by a factor of 40 compared to current measurements (Lellouch et al. 2011). Cooling by HCN is also discussed in this paper. It appears to be a possible alternative solution, but only if it remains largely supersaturated in the mesosphere.

Changing the temperature boundary condition may suppress the negative gradient, but at the expense of creating a warm, unexplained thermal profile above 1,350 km. We have investigated more exotic solutions, like zonal winds or compositional variations that would "unbend" the retrieved temperature profiles, allowing a more isothemal mesosphere. However, no realistic models could be built upon those alternative assump-

tions. Again, the *New Horizons* flyby will provide constraints on the temperature boundary conditions and atmospheric composition that will be used to discriminate between the various solutions decribed here.

Acknowledgements. We acknowledge support from the French grants "Beyond Neptune" ANR-08-BLAN-0177 and "Beyond Neptune II" ANR-11-IS56-0002.

TRAPPIST is a project funded by the Belgian Fund for Scientific Research (F.R.S.-FNRS) under grant FRFC 2.5.594.09.F, with the participation of the Swiss National Science Foundation.

J. L. Ortiz and N. Morales acknowledge funding from Proyecto de Excelencia de la Junta de Andalucía, J.A. 2012-FQM1776 and from FEDER funds.

M. Gillon and E. Jehin are F.R.S.-FNRS Research Associates.

C. Opitom acknowledge the support of the F.R.S.-FNRS for her PhD thesis.

R. Leiva is supported by CONICYT PCHA/Doctorado Nacional scholarship.

M. Assafin thanks the CNPq (Grants 473002/2013-2 and 308721/2011-0) and FAPERJ (Grant E-26/111.488/2013).

A. R. Gomes-Júnior thanks CAPES.

We also thank Caisey Harlingten, for the use of his 20 inch telescope in San Pedro de Atacama.

REFERENCES

Assafin, M., Camargo, J.I.B., Vieira Martins, R., Andrei, A.H., Sicardy, B., Young, L., da Silva Neto, D.N., Braga-Ribas, F., 2010. Precise predictions of stellar occultations by Pluto, Charon, Nix, and Hydra for 2008-2015. Astron. Astrophys. **515**, A32.

Assafin, M., Campos, R.P., Vieira Martins, R., da Silva Neto, D.N., Camargo, J.I.B., Andrei, A.H., 2008. Instrumental and digital coronagraphy for the observation of the Uranus satellites upcoming mutual events. Planetary and Space Science **56**, 1882–1887.

Assafin, M., Vieira-Martins, R., Braga-Ribas, F., Camargo, J.I.B., da Silva Neto, D.N., Andrei, A.H., 2009. Observations and Analysis of Mutual Events between the Uranus Main Satellites. Astron. Journal **137**, 4046–4053.

Baum, W.A., Code, A.D., 1953. A photometric observation of the occultation of σ ARIETIS by Jupiter. Astron. J. **58**, 108–112.

Benedetti-Rossi, G., Vieira Martins, R., Camargo, J.I.B., Assafin, M., Braga-Ribas, F., 2014. Pluto: improved astrometry from 19 years of observations. Astron. Astrophys. **570**, A86.

Bosh, A.S., Person, M.J., Levine, S.E., Zuluaga, C.A., Zangari, A.M., Gulbis, A.A.S., Schaefer, G.H., Dunham, E.W., Babcock, B.A., Davis, A.B., Pasachoff, J.M., Rojo, P., Servajean, E., Förster, F., Oswalt, T., Batcheldor, D., Bell, D., Bird, P., Fey, D., Fulwider, T., Geisert, E., Hastings, D., Keuhler, C., Mizusawa, T., Solenski, P., Watson, B., 2015. The state of Pluto's atmosphere in 2012-2013. Icarus **246**, 237–246.

Boursier, C., Ménard, J., Doyennette, L., Menard-Bourcin, F., 2003. Rovibrational Relaxation of Methane in Ch4-N2 Mixtures: Time-Resolved IR-IR Double-Resonance Measurements at 193 K and Kinetic Modeling. The Journal of Physical Chemistry A **107**, 5280–5290.

Braga-Ribas, F., Sicardy, B., Ortiz, J.L., Lellouch, E., Tancredi, G., Lecacheux, J., Vieira-Martins, R., Camargo, J.I.B., Assafin, M., Behrend, R., Vachier, F., Colas, F., Morales, N., Maury, A., Emilio, M., Amorim, A., Unda-Sanzana, E., Roland, S., Bruzzone, S., Almeida, L.A., Rodrigues, C.V., Jacques, C., Gil-Hutton, R., Vanzi, L., Milone, A.C., Schoenell, W., Salvo, R., Almenares, L., Jehin, E., Manfroid, J., Sposetti, S., Tanga, P., Klotz, A., Frappa, E., Cacella, P., Colque, J.P., Neves, C., Alvarez, E.M., Gillon, M., Pimentel, E., Giacchini, B., Roques, F., Widemann, T., Magalhães, V.S., Thirouin, A., Duffard, R., Leiva, R., Toledo, I., Capeche, J., Beisker, W., Pollock, J., Cedeño Montaña, C.E., Ivarsen, K., Reichart, D., Haislip, J., Lacluyze, A., 2013. The Size, Shape, Albedo, Density, and Atmospheric Limit of Transneptunian Object (50000) Quaoar from Multi-chord Stellar Occultations. The Astrophysichal Journal **773**, 26.

Brosch, N., 1995. The 1985 stellar occultation by Pluto. Mon. Not. R. Astron. Soc. **276**, 571–578.

Elliot, J.L., Ates, A., Babcock, B.A., Bosh, A.S., Buie, M.W., Clancy, K.B., Dunham, E.W., Eikenberry, S.S., Hall, D.T., Kern, S.D., Leggett, S.K., Levine, S.E., Moon, D.S., Olkin, C.B., Osip, D.J., Pasachoff, J.M., Penprase, B.E., Person, M.J., Qu, S., Rayner, J.T., Roberts, L.C., Salyk, C.V., Souza, S.P., Stone, R.C., Taylor, B.W., Tholen, D.J., Thomas-Osip, J.E., Ticehurst, D.R., Wasserman, L.H., 2003. The recent expansion of Pluto's atmosphere. Nature **424**, 165–168.

Elliot, J.L., Dunham, E.W., Bosh, A.S., Slivan, S.M., Young, L.A., Wasserman, L.H., Millis, R.L., 1989. Pluto's atmosphere. Icarus **77**, 148–170.

Elliot, J.L., Person, M.J., Gulbis, A.A.S., Souza, S.P., Adams, E.R., Babcock, B.A., Gangestad, J.W., Jaskot, A.E., Kramer, E.A., Pasachoff, J.M., Pike, R.E., Zuluaga, C.A., Bosh, A.S., Dieters, S.W., Francis, P.J., Giles, A.B., Greenhill, J.G., Lade, B., Lucas, R., Ramm, D.J., 2007. Changes in Pluto's Atmosphere: 1988-2006. Astron. J. **134**, 1–13.

Fray, N., Schmitt, B., 2009. Sublimation of ices of astrophysical interest: A bibliographic review. Planetary and Space Science **57**, 2053–2080.

French, R.G., Toigo, A.D., Gierasch, P.J., Hansen, C.J., Young, L.A., Sicardy, B., Dias-Oliveira, A., Guzewich, S.D., 2015. Seasonal variations in Pluto's atmospheric tides. Icarus **246**, 247–267.

Gulbis, A.A.S., Emery, J.P., Person, M.J., Bosh, A.S., Zuluaga, C.A., Pasachoff, J.M., Babcock, B.A., 2015. Observations of a successive stellar occultation by Charon and graze by Pluto in 2011: Multiwavelength SpeX and MORIS data from the IRTF. Icarus **246**, 226–236.

Hansen, C.J., Paige, D.A., 1996. Seasonal Nitrogen Cycles on Pluto. Icarus **120**, 247–265.

Hubbard, W.B., Hunten, D.M., Dieters, S.W., Hill, K.M., Watson, R.D., 1988. Occultation evidence for an atmosphere on Pluto. Nature **336**, 452–454.

Jehin, E., Gillon, M., Queloz, D., Magain, P., Manfroid, J., Chantry, V., Lendl, M., Hutsemékers, D., Udry, S., 2011. TRAPPIST: TRAnsiting Planets and PlanetesImals Small Telescope. The Messenger **145**, 2–6.

Krasnopolsky, V.A., Cruikshank, D.P., 1999. Photochemistry of Pluto's atmosphere and ionosphere near perihelion. Journal of Geophysical Reserach **104**, 21979–21996.

Lara, L.M., Ip, W.H., Rodrigo, R., 1997. Photochemical Models of Pluto's Atmosphere. Icarus **130**, 16–35.

Lellouch, E., Bézard, B., Flasar, F.M., Vinatier, S., Achterberg, R., Nixon, C.A., Bjoraker, G.L., Gorius, N., 2014. The distribution of methane in Titans stratosphere from Cassini/CIRS observations. Icarus **231**, 323–337.

Lellouch, E., 1994. The thermal structure of Pluto's atmosphere: Clear VS hazy models. Icarus **108**, 255–264.

Lellouch, E., Laureijs, R., Schmitt, B., Quirico, E., de Bergh, C., Crovisier, J., Coustenis, A., 2000. Pluto's Non-isothermal Surface. Icarus **147**, 220–250.

Lellouch, E., Sicardy, B., de Bergh, C., Käufl, H.U., Kassi, S., Campargue, A., 2009. Pluto's lower atmosphere structure and methane abundance from high-resolution spectroscopy and stellar occultations. Astron. Astrophys. **495**, L17–L21.

Lellouch, E., Stansberry, J., Emery, J., Grundy, W., Cruikshank, D.P., 2011. Thermal properties of Pluto's and Charon's surfaces from Spitzer observations. Icarus **214**, 701–716.

Lellouch, E., Santos-Sanz, P., Lacerda, P., Mommert, M., Duffard, R., Ortiz, J. L., Müller, T. G., Fornasier, S., Stansberry, J., Kiss, C., Vilenius, E., Mueller, M., Peixinho, N., Moreno, R., Groussin, O., Delsanti, A., Harris, A. W., 2013. "TNOs are Cool'": A survey of the trans-Neptunian region. IX. Thermal properties of Kuiper belt objects and Centaurs from combined Herschel and Spitzer observations. Astron. Astrophys. **557**, A60.

Lellouch, E., de Bergh, C., Sicardy, B., Forget, F., Vangvichith, M., Käufl, H.-U., 2015. Exploring the spatial, temporal, and vertical distribution of methane in Pluto's atmosphere. Icarus **246**, 268–278.

Lenzen, R., Hartung, M., Brandner, W., Finger, G., Hubin, N.N., Lacombe, F., Lagrange, A.M., Lehnert, M.D., Moorwood, A.F.M., Mouillet, D., NAOS-CONICA first on sky results in a variety of observing modes. in: Instrument Design and Performance for Optical/Infrared Ground-based Telescopes, (Eds.) M. Iye, A.F.M. Moorwood vol. 4841 of *Society of Photo-Optical Instrumentation Engineers (SPIE) Conference Series* 2003 pp. 944–952.

Olkin, C.B., Young, L.A., Borncamp, D., Pickles, A., Sicardy, B., Assafin, M., Bianco, F.B., Buie, M.W., de Oliveira, A.D., Gillon, M., French, R.G., Ramos Gomes, A., Jehin, E., Morales, N., Opitom, C., Ortiz, J.L., Maury, A., Norbury, M., Braga-Ribas, F., Smith, R., Wasserman, L.H., Young, E.F., Zacharias, M., Zacharias, N., 2015. Evidence that Pluto's atmosphere does not collapse from occultations including the 2013 May 04 event. Icarus **246**, 220–225.

Olkin, C.B., Young, L.A., French, R.G., Young, E.F., Buie, M.W., Howell, R.R., Regester, J., Ruhland, C.R., Natusch, T., Ramm, D.J., 2014. Pluto's atmospheric structure from the July 2007 stellar occultation. Icarus **239**, 15–22.

Ortiz, J.L., Sicardy, B., Braga-Ribas, F., Alvarez-Candal, A., Lellouch, E., Duffard, R., Pinilla-Alonso, N., Ivanov, V.D., Littlefair, S.P., Camargo, J.I.B., Assafin, M., Unda-Sanzana, E., Jehin, E., Morales, N., Tancredi, G., Gil-Hutton, R., de La Cueva, I., Colque, J.P., da Silva Neto, D.N., Manfroid, J., Thirouin, A., Gutiérrez, P.J., Lecacheux, J., Gillon, M., Maury, A., Colas, F., Licandro, J., Mueller, T., Jacques, C., Weaver, D., Milone, A., Salvo, R., Bruzzone, S., Organero, F., Behrend, R., Roland,

S., Vieira-Martins, R., Widemann, T., Roques, F., Santos-Sanz, P., Hestroffer, D., Dhillon, V.S., Marsh, T.R., Harlingten, C., Campo Bagatin, A., Alonso, M.L., Ortiz, M., Colazo, C., Lima, H.J.F., Oliveira, A.S., Kerber, L.O., Smiljanic, R., Pimentel, E., Giacchini, B., Cacella, P., Emilio, M., 2012. Albedo and atmospheric constraints of dwarf planet Makemake from a stellar occultation. Nature **491**, 566–569.

Person, M.J., Dunham, E.W., Bosh, A.S., Levine, S.E., Gulbis, A.A.S., Zangari, A.M., Zuluaga, C.A., Pasachoff, J.M., Babcock, B.A., Pandey, S., Amrhein, D., Sallum, S., Tholen, D.J., Collins, P., Bida, T., Taylor, B., Bright, L., Wolf, J., Meyer, A., Pfueller, E., Wiedemann, M., Roeser, H.P., Lucas, R., Kakkala, M., Ciotti, J., Plunkett, S., Hiraoka, N., Best, W., Pilger, E.J., Micheli, M., Springmann, A., Hicks, M., Thackeray, B., Emery, J.P., Tilleman, T., Harris, H., Sheppard, S., Rapoport, S., Ritchie, I., Pearson, M., Mattingly, A., Brimacombe, J., Gault, D., Jones, R., Nolthenius, R., Broughton, J., Barry, T., 2013. The 2011 June 23 Stellar Occultation by Pluto: Airborne and Ground Observations. Astron. Journal **146**, 83.

Press, W.H., Teukolsky, S.A., Vetterling, W.T., Flannery, B.P., *Numerical recipes in C. The art of scientific computing* 1992.

Rousset, G., Lacombe, F., Puget, P., Hubin, N.N., Gendron, E., Fusco, T., Arsenault, R., Charton, J., Feautrier, P., Gigan, P., Kern, P.Y., Lagrange, A.M., Madec, P.Y., Mouillet, D., Rabaud, D., Rabou, P., Stadler, E., Zins, G., NAOS, the first AO system of the VLT: on-sky performance. in: Adaptive Optical System Technologies II, (Eds.) P.L. Wizinowich, D. Bonaccini vol. 4839 of *Society of Photo-Optical Instrumentation Engineers (SPIE) Conference Series* 2003 pp. 140–149.

Sicardy, B., Bellucci, A., Gendron, E., Lacombe, F., Lacour, S., Lecacheux, J., Lellouch, E., Renner, S., Pau, S., Roques, F., Widemann, T., Colas, F., Vachier, F., Martins, R.V., Ageorges, N., Hainaut, O., Marco, O., Beisker, W., Hummel, E., Feinstein, C., Levato, H., Maury, A., Frappa, E., Gaillard, B., Lavayssière, M., di Sora, M., Mallia, F., Masi, G., Behrend, R., Carrier, F., Mousis, O., Rousselot, P., Alvarez-Candal, A., Lazzaro, D., Veiga, C., Andrei, A.H., Assafin, M., da Silva Neto, D.N., Jacques, C., Pimentel, E., Weaver, D., Lecampion, J.F., Doncel, F., Momiyama, T., Tancredi, G., 2006. Charon's size and an upper limit on its atmosphere from a stellar occultation. Nature **439**, 52–54.

Sicardy, B., Ferri, F., Roques, F., Lecacheux, J., Pau, S., Brosch, N., Nevo, Y., Hubbard, W.B., Reitsema, H.J., Blanco, C., Carreira, E., Beisker, W., Bittner, C., Bode, H.J., Bruns, M., Denzau, H., Nezel, M., Riedel, E., Struckmann, H., Appleby, G., Forrest, R.W., Nicolson, I.K.M., Hollis, A.J., Miles, R., 1999. The Structure of Titan's Stratosphere from the 28 Sgr Occultation. Icarus **142**, 357–390.

Sicardy, B., Ortiz, J.L., Assafin, M., Jehin, E., Maury, A., Lellouch, E., Hutton, R.G., Braga-Ribas, F., Colas, F., Hestroffer, D., Lecacheux, J., Roques, F., Santos-Sanz, P., Widemann, T., Morales, N., Duffard, R., Thirouin, A., Castro-Tirado, A.J., Jelínek, M., Kubánek, P., Sota, A., Sánchez-Ramírez, R., Andrei, A.H., Camargo, J.I.B., da Silva Neto, D.N., Gomes, A.R., Martins, R.V., Gillon, M., Manfroid, J., Tozzi, G.P., Harlingten, C., Saravia, S., Behrend, R., Mottola, S., Melendo, E.G., Peris, V., Fabregat, J., Madiedo, J.M., Cuesta, L., Eibe, M.T., Ullán, A., Organero, F., Pastor, S., de Los Reyes, J.A., Pedraz, S., Castro, A., de La Cueva, I., Muler, G., Steele, I.A., Cebrián, M., Montañés-Rodríguez, P., Oscoz, A., Weaver, D., Jacques, C., Corradi, W.J.B., Santos, F.P., Reis, W., Milone, A., Emilio, M., Gutiérrez, L., Vázquez, R., Hernández-Toledo, H., 2011. A Pluto-like radius and a high albedo for the dwarf planet Eris from an occultation. Nat **478**, 493–496.

Sicardy, B., Widemann, T., Lellouch, E., Veillet, C., Cuillandre, J.C., Colas, F., Roques, F., Beisker, W., Kretlow, M., Lagrange, A.M., Gendron, E., Lacombe, F., Lecacheux, J., Birnbaum, C., Fienga, A., Leyrat, C., Maury, A., Raynaud, E., Renner, S., Schultheis, M., Brooks, K., Delsanti, A., Hainaut, O.R., Gilmozzi, R., Lidman, C., Spyromilio, J., Rapaport, M., Rosenzweig, P., Naranjo, O., Porras, L., Díaz, F., Calderón, H., Carrillo, S., Carvajal, A., Recalde, E., Cavero, L.G., Montalvo, C., Barría, D., Campos, R., Duffard, R., Levato, H., 2003. Large changes in Pluto's atmosphere as revealed by recent stellar occultations. Nature **424**, 168–170.

Siddles, R., Wilson, G., Simpson, C., 1994. The vibrational deactivation of the (0001) mode of {N2O} measured down to 150 K. Chemical Physics Letters **225**, 146 – 149.

Strobel, D.F., Zhu, X., Summers, M.E., Stevens, M.H., 1996. On the Vertical Thermal Structure of Pluto's Atmosphere. Icarus **120**, 266–289.

Summers, M.E., Strobel, D.F., Gladstone, G.R., *Chemical Models of Pluto's Atmosphere* 1997 p. 391 p. 391.

Tholen, D.J., Buie, M.W., Grundy, W.M., Elliott, G.T., 2008. Masses of Nix and Hydra. AJ, **135**, 777.

Vangvichith, M., 2013. Modélisation des atmosphères et des glaces de Pluton et Triton. Thèse de Doctorat, Ecole Polytechnique, France **000**.

Vapillon, L., Combes, M., Lecacheux, J., 1973. The beta Scorpii occultation by Jupiter. II. The temperature and density profiles of the Jupiter upper atmosphere.. Astron. Astrophys. **29**, 135–149.

Vuitton, V., Yelle, R.V., McEwan, M.J., 2007. Ion chemistry and N-containing molecules in Titan's upper atmosphere. Icarus **191**, 722–742.

Washburn, E.W., *International Critical Tables of Numerical Data: Physics, Chemistry and Technology.* Vol. 7, p. 11. McGraw-Hill, New York, 1930.

Yelle, R.V., 1991. Non-LTE models of Titan's upper atmosphere. Astron. Journal **383**, 380–400.

Yelle, R.V., Lunine, J.I., 1989. Evidence for a molecule heavier than methane in the atmosphere of Pluto. Nature **339**, 288–290.

Young, E.F., French, R.G., Young, L.A., Ruhland, C.R., Buie, M.W., Olkin, C.B., Regester, J., Shoemaker, K., Blow, G., Broughton, J., Christie, G., Gault, D., Lade, B., Natusch, T., 2008. Vertical Structure in Pluto's Atmosphere from the 2006 June 12 Stellar Occultation. Astron. Journal **136**, 1757–1769.

Young, L.A., 2013. Pluto's Seasons: New Predictions for New Horizons. Astrophys. J., Lett. **766**, L22.

Zacharias, N., Monet, D.G., Levine, S.E., Urban, S.E., Gaume, R., Wycoff, G.L., The Naval Observatory Merged Astrometric Dataset (NOMAD). in: American Astronomical Society Meeting Abstracts vol. 36 of *Bulletin of the American Astronomical Society* 2004 p. 1418.

Zalucha, A.M., Gulbis, A.A.S., Zhu, X., Strobel, D.F., Elliot, J.L., 2011a. An analysis of Pluto occultation light curves using an atmospheric radiative-conductive model. Icarus **211**, 804–818.

Zalucha, A.M., Michaels, T.I., 2013. A 3D general circulation model for Pluto and Triton with fixed volatile abundance and simplified surface forcing. Icarus **223**, 819–831.

Zalucha, A.M., Zhu, X., Gulbis, A.A.S., Strobel, D.F., Elliot, J.L., 2011b. An investigation of Pluto's troposphere using stellar occultation light curves and an atmospheric radiative-conductive-convective model. icarus **214**, 685–700.

Zhu, X., Strobel, D.F., Erwin, J.T., 2014. The density and thermal structure of Pluto's atmosphere and associated escape processes and rates. Icarus **228**, 301–314.

This preprint was prepared with the AAS LaTeX macros v5.2.

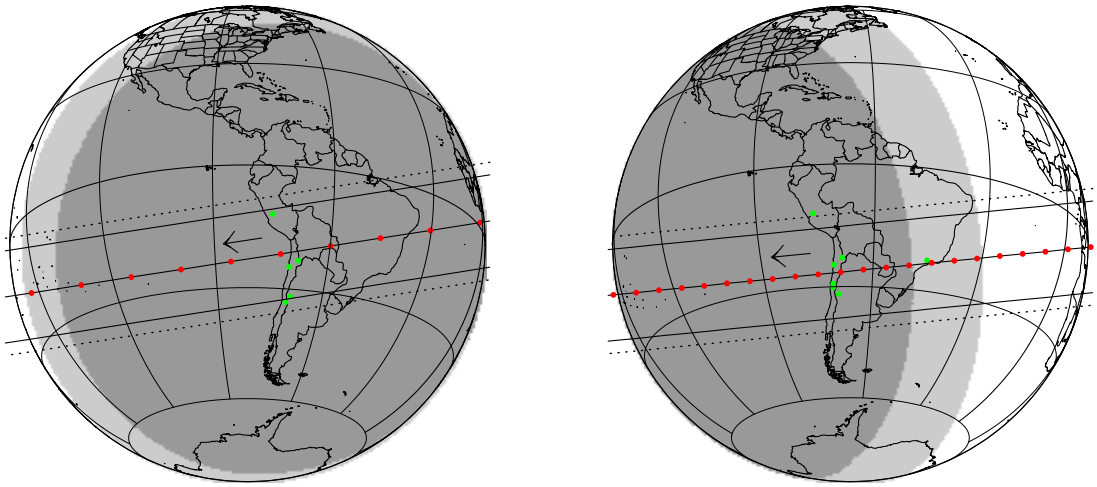

Fig. 1.— The post-occultation, reconstructed paths of Pluto's shadow for the two events studied here. The red dots indicate the shadow center every minute and the arrows show the direction of motion. The green dots mark the sites where data were obtained. The black solid lines correspond to the half-light stellar level, while the dotted lines correspond to the 1% stellar drop, thus marking the practical region of detectability of the occultations. Left - The 18 July 2012 event. The first red dot at right is at 04h 09m UT, the last one at left corresponds to 04h 18m UT. Right -The 4 May 2013 event. The first red dot at right is at 08h 12m UT, the last one at left corresponds to 08h 33m UT.

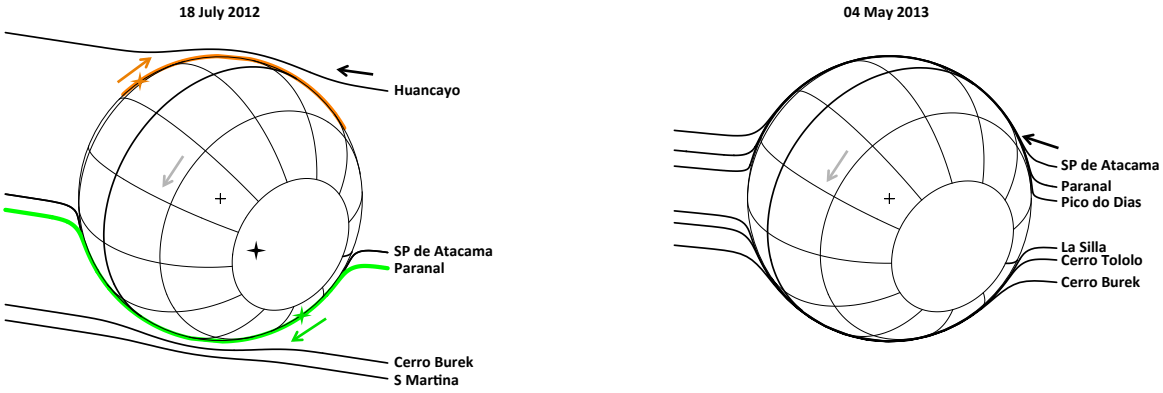

Fig. 2.— Left - The trajectories of the primary stellar images relative to Pluto, as seen from the five stations used on 18 July 2012, see Table 1. The black arrow shows the general direction of stellar motion. Here, Pluto's has an assumed radius $R_P = 1,190$ km (see text), and its center is indicated by the cross symbol. The gray arrow inside the disk indicates the direction of rotation. In the case of Paranal, we have plotted the path of the primary image in green, *and* the associated path of the secondary image in orange (see also Fig. 7). The green and orange arrows show the corresponding local stellar motion along Pluto's limb. Note that the two images move in opposite directions. The black star symbol shows the star position as seen from Paranal at a given, arbitrary moment, while the green and orange star symbols indicate the associated primary and seconday images at that time, respectively. Note that the three star symbols and the cross are aligned. Right - The same as left panel for the 04 May 2013 occultation, with only the paths of the primary stellar images plotted.

Table 1: Circumstances of the 18 July 2012 Pluto occultation

Site	Lat. (d:m:s) Lon. (d:m:s) alt (m)	Telescope Instrument/filter	Exp. time/cycle(s)[1]	Observers
Observatory UC (Santa Martina)	33:16:09.0 S 70:32:04.0 W 1,450	0.4 m CCD/clear	1.0/1.0	R. Leiva Espinoza
Cerro Burek	31:47:12.4 S 69:18:24.5 W 2,591	ASH 0.45 m SBIG-STL11000/clear	13.0/15.7	N. Morales
Paranal	24:37:31.0 S 70:24:08.0 W 2,635	VLT Yepun 8.2 m NACO/H	0.2/0.2	J. Girard
San Pedro de Atacama	22:57:12.3 S 68:10:47.6 W 2,397	ASH2 0.4 m SBIG-STL11000/clear	13.0/15.44	N. Morales
Huancayo	12:02:32.2 S 75:19:14.7 W 3,344	0.2 m CCD/clear	10.24/10.24[2] 5.12/5.12[2]	E. Meza

Notes. [1]Cycle is defined as the exposure time plus the readout time (called dead time).
[2]Exposure time was changed at 04:11:46 UT

Table 2: Circumstances of the 04 May 2013 Pluto occultation

Site	Lat. (d:m:s) Lon. (d:m:s) alt meters	Telescope Instrument/filter	Exposure time (s) Cycle (s)	Observers
Cerro Burek	31:47:12.4 S 69:18:24.5 W 2,591 m	ASH 0.45m SBIG-STL11000/clear	6/8	J.L. Ortiz N. Morales
CASLEO (Leoncito)	31:47:55.6 S 69:17:44.9 W 2,492 m	Jorge Sahade 2.15m CCD/R	5/6.8	R. Gil-Hutton C. Lopez-Sisterna
Cerro Tololo	30:10:03.4 S 70:48:19.0 W 2,207	PROMPT 0.4m P1, P3, P4, P5 CCD/clear	5/8 P3 offset 2 sec P4 offset 4 sec P5 offset 6 sec	J. Pollock
La Silla	29 15 21.276 S 70 44 20.184 W 2,336	Danish 1.54m Lucky Imager/Z ($\lambda > 650$nm CCD/iXon response)	0.1/0.1 several interruptions due to image cube writing	L. Mancini
La Silla	29 15 16.59 S 70 44 21.82 W 2,315	TRAPPIST[1] 0.6m CCD/clear	4.5/6	E. Jehin, A. Decock, M. Gillon C. Opitom
Pico dos Dias	22 32 07.8 S 45 34 57.7 W 1,811	B&C 0.6m CCD/I	5/5.40	M. Assafin, A. Ramos-Gomes Jr
Ponta Grossa	25 05 24.00 S 50 09 36.00 W 909	M16 0.4m CCD/clear	5 Tecnichal Problems	M. Emilio
Cerro Paranal	24:37:31.0 S 70:24:08.0 W 2,635	UT4 Yepun 8.2m NACO/H	0.2/0.2	G. Hau
San Pedro de Atacama	22:57:12.3 S 68:10:47.6 W 2,397	Caisey 0.5m f/8 CCD/V	3/4.58	A. Maury
	–	Caisey 0.5m f/6.8 CCD/B	4/4.905	L. Nagy
	–	CAO 0.4m CCD/R	4/6.35	J.F. Soulier
	–	ASH2 0.4m	STL11000 technical problem	N. Morales
	–	OPSPA 0.3m CCD/clear	5/11.1	J. Fabrega Polleri
Huancayo	12:02:32.2 S 75:19:14.7 W 3,344	0.2 m CCD/clear	10.24/10.24 Negative chord	E. Meza

Notes. [1]Jehin et al. (2011)

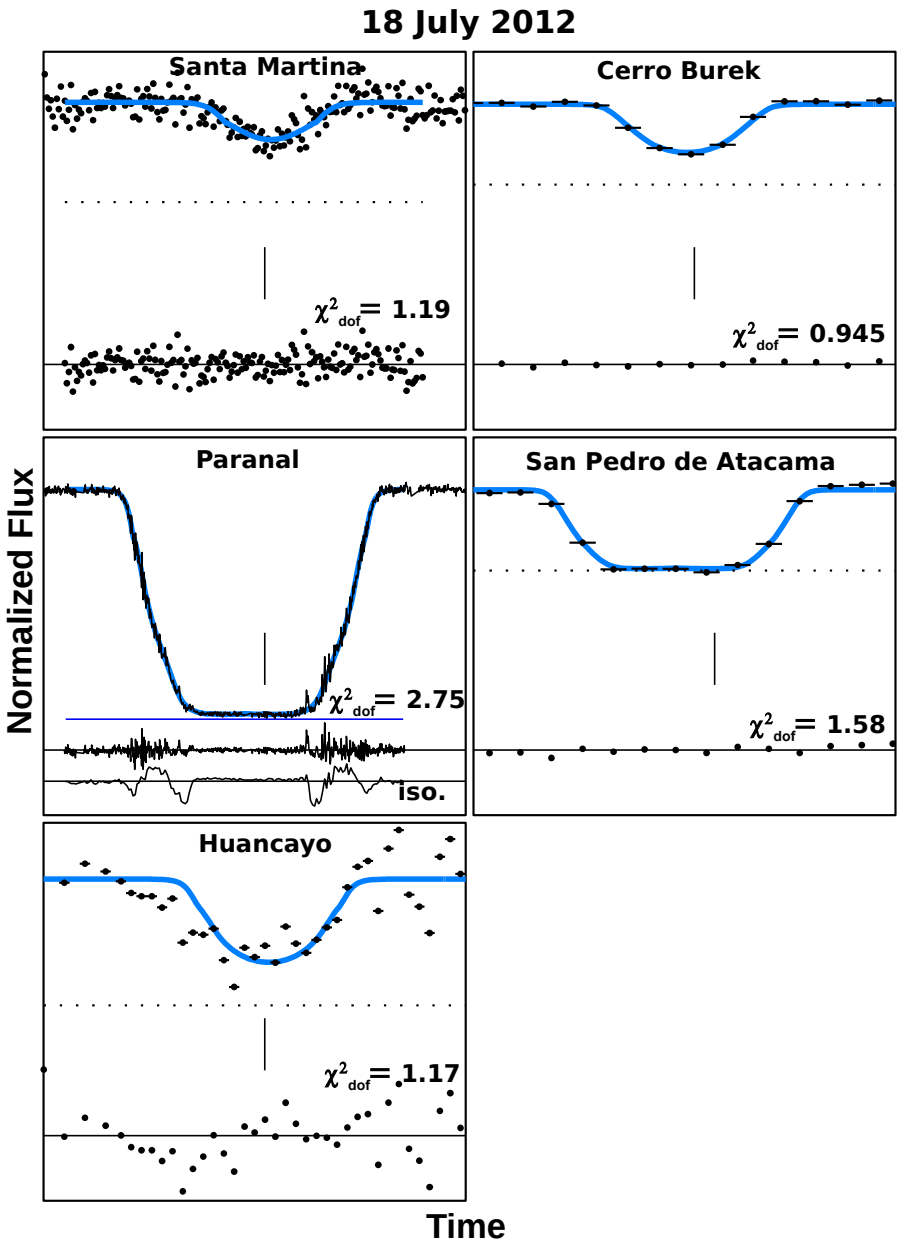

Fig. 3.— The blue curves are a simultaneous fit to the 18 July 2012 light-curves, using the best atmospheric model described in Table 4 and Fig. 13. The number at the lower right of each panel is the value of $\chi^2_{\rm dof}$ (Eq. A8), i.e. the χ^2 per degree of freedom for each corresponding fits. Each panel spans 3 minutes of data, with the vertical tick marks located at 04:13 UT. All the light curves show the total flux (star+Pluto+Charon) plotted at the same vertical scale. The horizontal bars on the Cerro Burek, San Pedro de Atacama and Huancayo data points represent the respective integration times. The zero flux is indicated by the solid horizontal line at the bottom of each panel, together with the residuals (data minus model). The dotted horizontal lines mark the *fitted* zero stellar fluxes (or equivalently, the Pluto+Charon contribution to the total flux), obtained using our best Pluto atmospheric model. The blue horizontal line in the Paranal panel marks the *measured* zero stellar flux at that station, the only one at which a photometric calibration was possible (see text and Figs. 6, 7). In the Paranal panel, we have also added the residuals (labelled "iso.") obtained by forcing an isothermal mesosphere at $T_{\rm iso}$ = 95.5 K. The residuals have been averaged over 5-s time intervals and shifted vertically by -0.12 for better showing the clear discrepancy between the isothermal mesospheric model and the data. Other values chosen for $T_{\rm iso}$ would result in the same qualitative behavior. In essence, isothermal mesospheres do not provide satisfactory fits to the NACO light-curve.

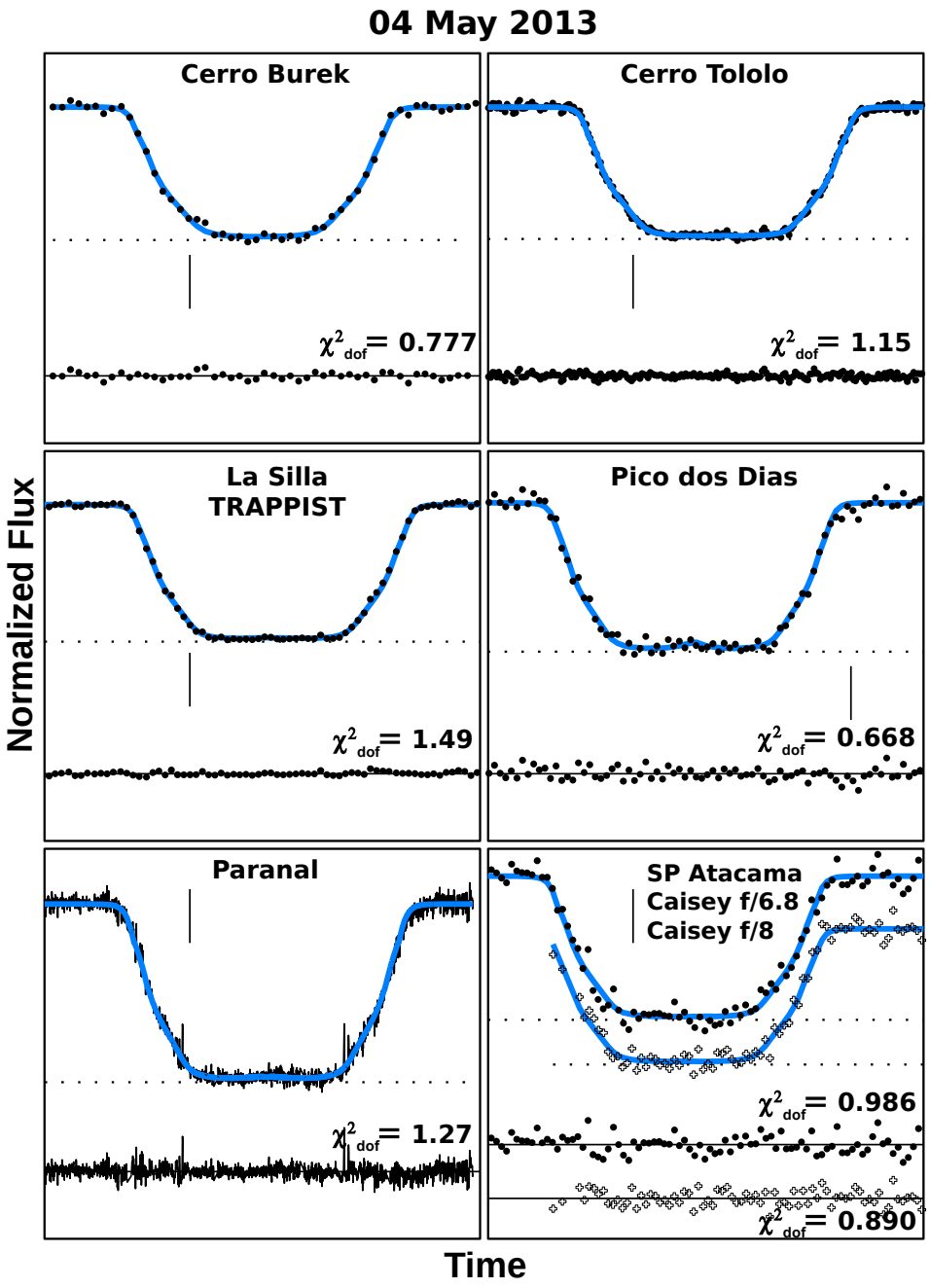

Fig. 4.— The same as Fig. 3 for the 04 May 2013 event. Each panel now represents 6 minutes of data, with the vertical tick mark located at 08:22 UT. Note that the two light-curves from San Pedro ("SP") de Atacama have been displaced vertically by ±0.1 for better viewing.

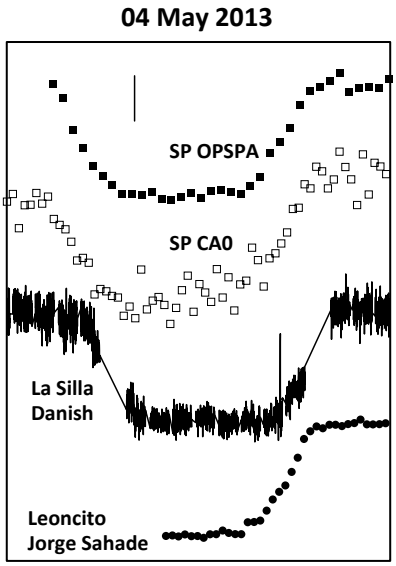

Fig. 5.— The same as Fig. 4, but for the light-curves that were not included in the fit, either due to lower SNR, or interruptions during the acquisition. See Table 2 for intrumental details ("SP" refers to San Pedro de Atacama and acronyms refer to telescope used in that station.). Note that the Leoncito, Danish and SP light-curves duplicate the observations of the Cerro Burek, La Silla TRAPPIST and Caisey telescopes, respectively.

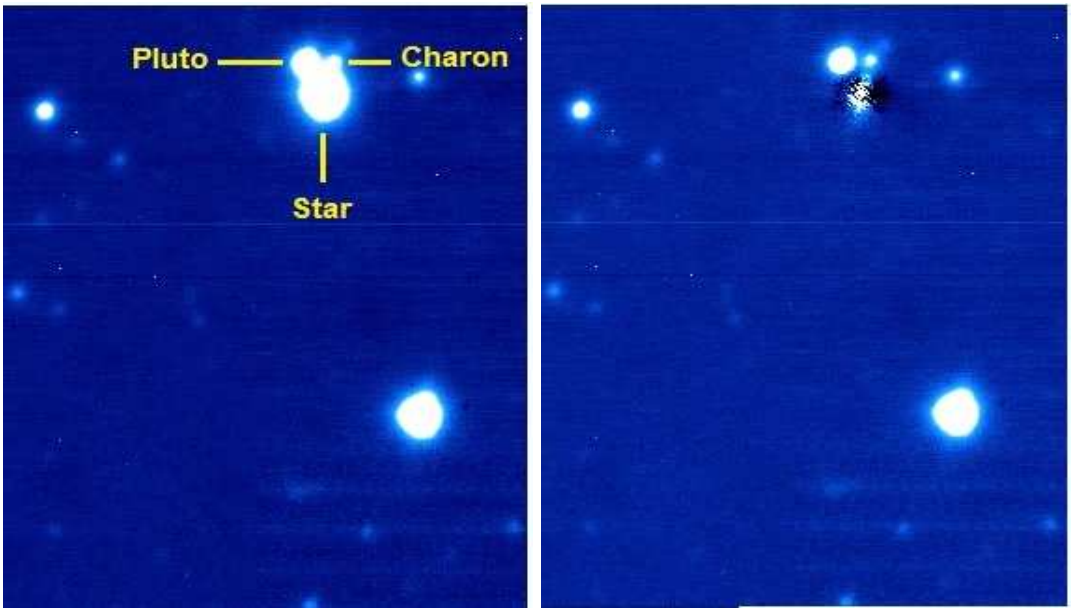

Fig. 6.— Photometric calibration of the July 18, 2012 event (Paranal/VLT, NACO H-band). Left - Image taken some 20 minutes before the event, showing the small separation between Pluto, Charon and the star ($\sim$ 1"). Right - The same image after a digital coronagraphy treatment that removed the stellar image. See text for details.

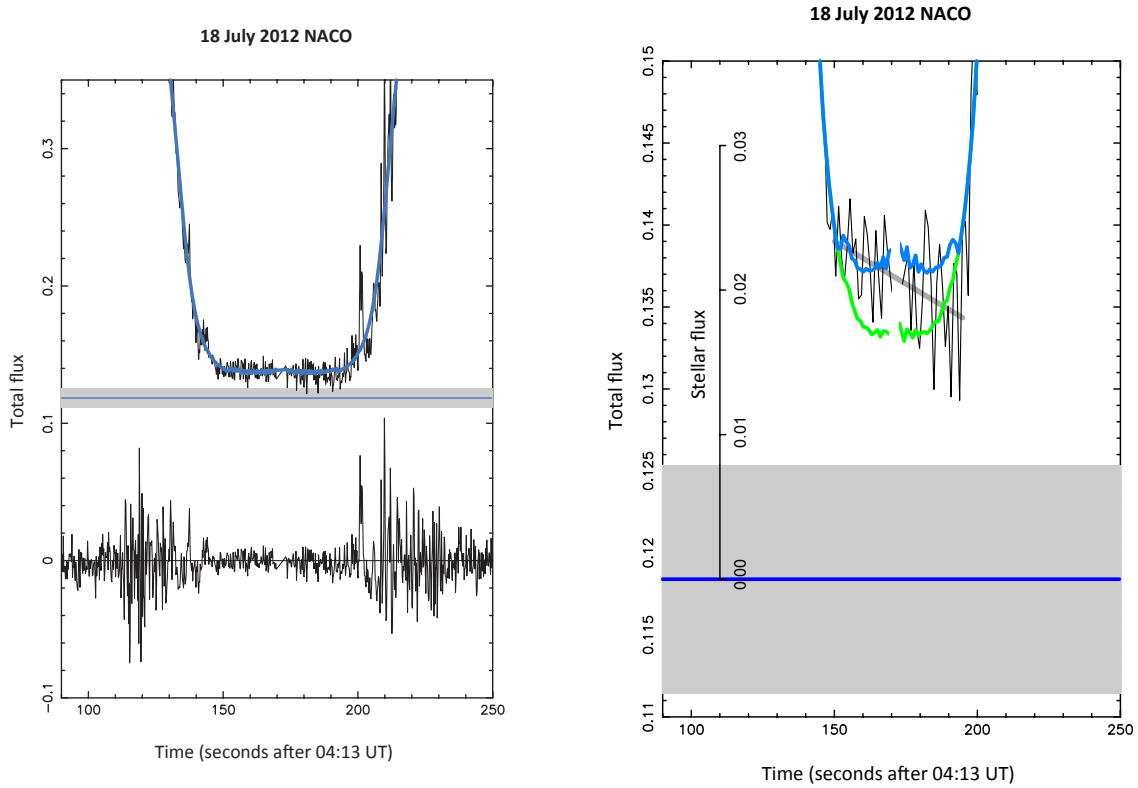

Fig. 7.— Left - details of the fit to the NACO 18 July 2012 light-curve (see also the middle-left panel of Fig. 3). The horizontal blue line in the gray shaded area indicates the Pluto + Charon contribution to the total observed flux and its 1-σ error bar, 0.1184 ± 0.007. The residuals curve at the bottom clearly shows the spike activity at ingress and egress. Right - Expanded view of the left panel. The data have been binned over 1 sec-time intervals to better show the flux decrease during the central phase of the occultation. The flux of the *primary* stellar image is plotted in green, while the blue curve is the sum of the primary and secondary images, according to the model (see Fig. 2 and Appendix). Thus, the contribution of the secondary image is the difference between the blue and green curves. Note the interruption of data acquisition (about 3 sec) at mid-occultation, necessary to the writing of the data cube before the start of the next data cube. The inclined gray line is a linear fit to the central part of the light-curve, which illustrates the ingress/egress asymmetry of the residual stellar flux. The vertical axis inside the box at left indicates the value of the residual, normalized stellar flux. It shows that the stellar flux decreased from about 2.3% to about 1.8% of its full unocculted value during that interval. The systematic error on those values is ±0.8% (corresponding to the shaded area).

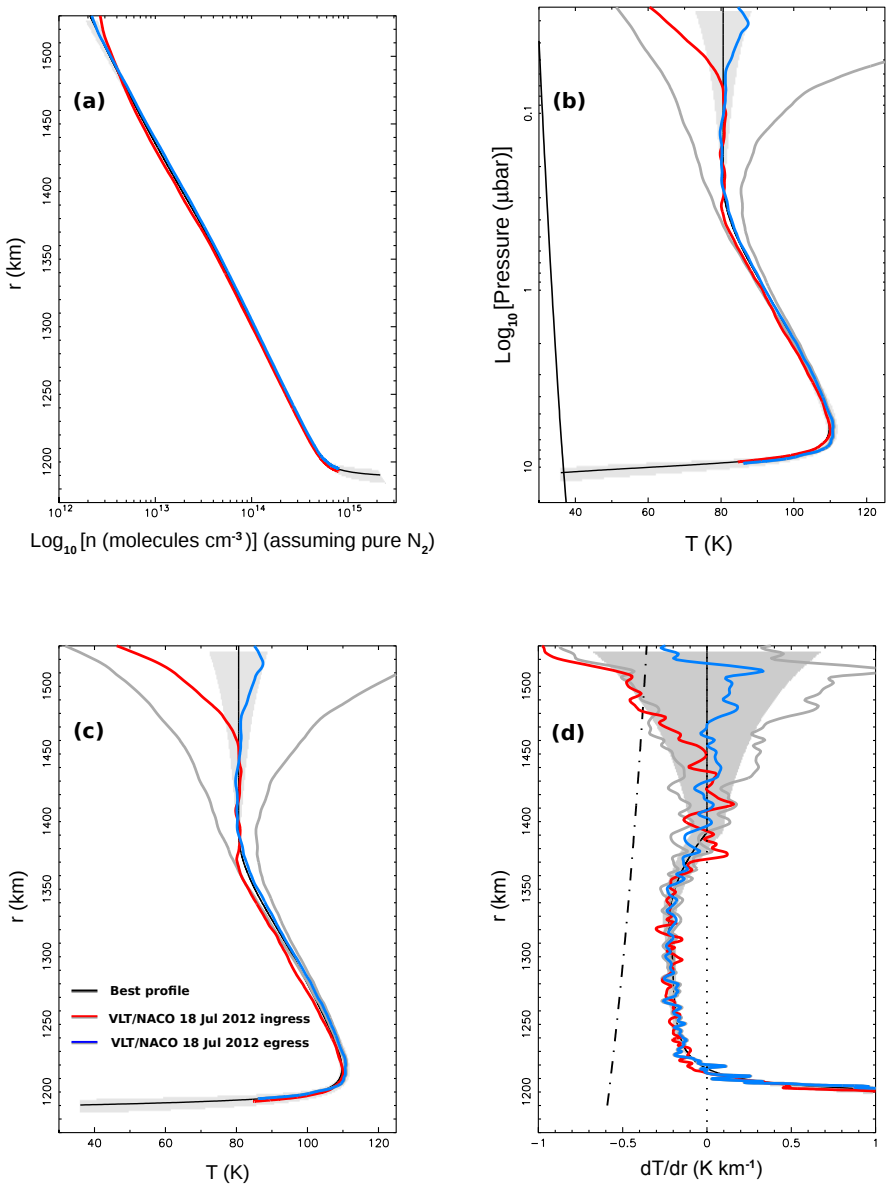

Fig. 8.— In all the panels, the black solid line is the model that best fits all the 18 July 2012 NACO light-curves, see Figs. 3 and Table 4. The red (resp. blue) lines are the particular profiles obtained from the inversion of the NACO 18 July 2012 light-curve at ingress/summer (resp. egress/winter). The shaded areas at the top of the profiles indicate the expected $\pm 1\sigma$ fluctuations caused by the photometric noise, see text. The shaded areas at the bottom of the profiles are the $\pm 1\sigma$ uncertainty domain caused by the uncertainty on the Pluto + Charon contribution to the 18 July 2012 NACO light-curve, see Fig. 7. (a) Molecular density vs. radius (assuming a pure N_2 atmosphere); (b) temperature vs. pressure; (c) temperature vs. radius; (d) temperature gradient vs. radius. The two gray temperature profiles in panels (b), (c) and (d) show the effect of different temperature boundary conditions for the egress NACO profile. More precisely, those profiles differ from the nominal one (blue lines) by ± 5 K at 1,390 km. The oblique solid line at the left of panel (b) is the vapor pressure equilibrium limit for N_2 (Fray and Schmitt 2009). Nitrogen should condense at the left of this line, so that its intersection with the temperature profile may define Pluto's surface in the absence of troposphere, see Fig. 9 and text for details. The dash-dotted line in panel (d) is the dry adiabat for a pure N_2 atmosphere.

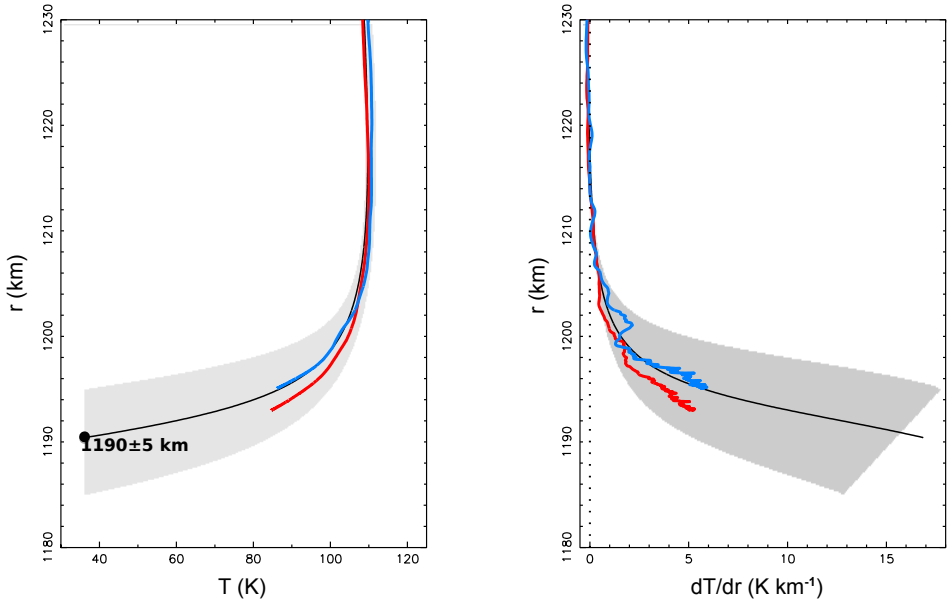

Fig. 9.— Left - Expanded view of the bottom of the temperature profiles shown in Fig. 8. The bullet is the intersection with the nitrogen condensation line. The error bar attached to its positions is defined by the radial extension of the shaded uncertainty domain. Right - The corresponding expanded view for the temperature gradient.

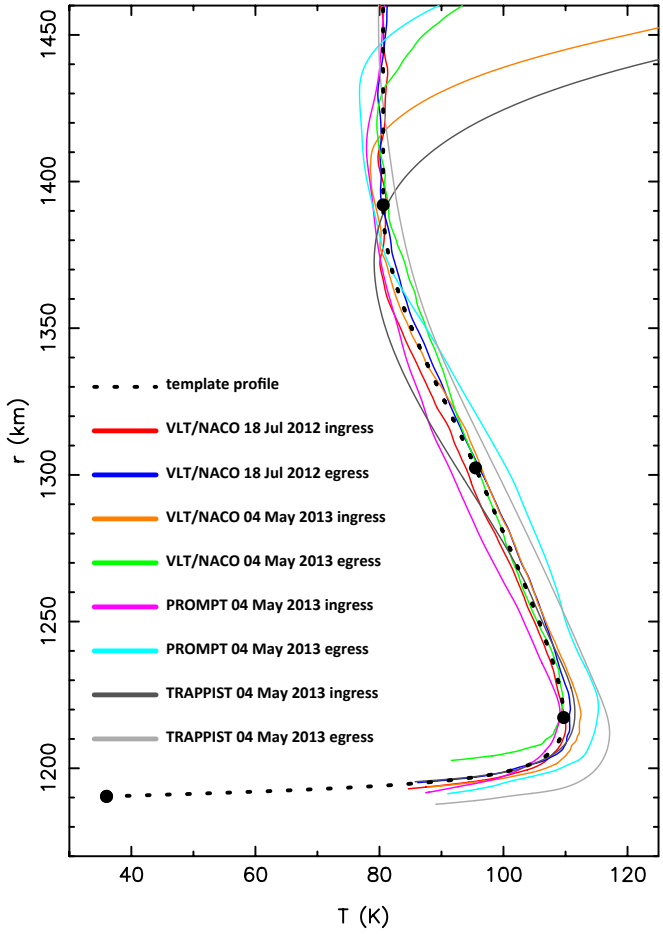

Fig. 10.— The temperature profiles derived from the inversion of our best occultation light-curves obtained on 18 July 2012 and 04 May 2013. The dotted line is our global, best-fitting temperature profile (also shown in Figs. 8 and 13).

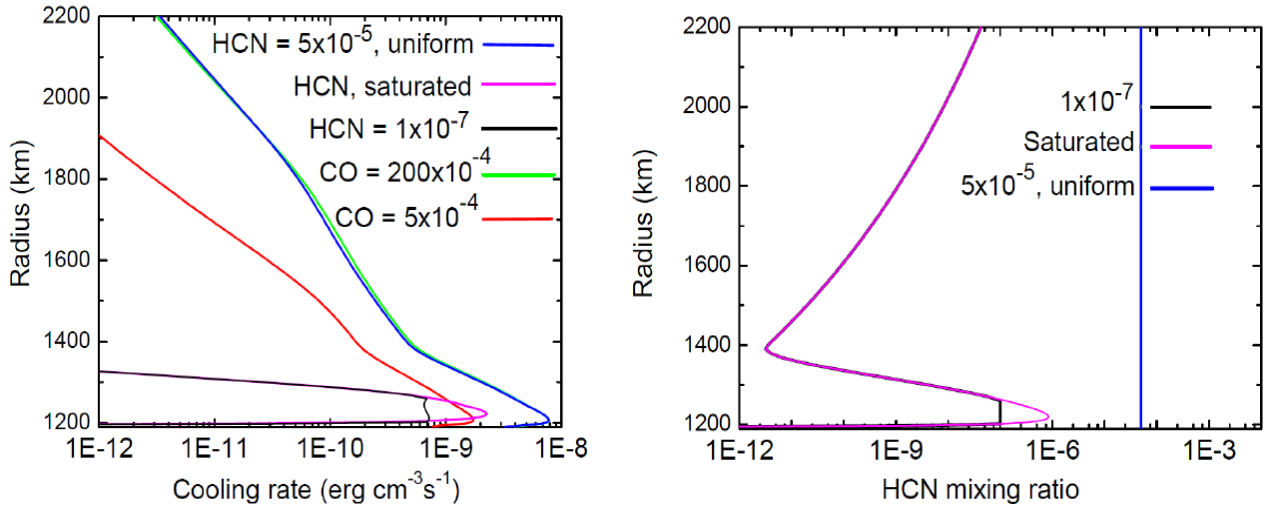

Fig. 11.— Calculation of cooling rates by CO and HCN. The y-axis is the distance from Pluto's center, with the surface position assumed here at 1,184 km. Left panel - Cooling rates assuming the thermal profile from this work. Red and green curves: CO cooling rates for $q_{\rm CO} = 5 \times 10^{-4}$ and 200×10^{-4}, respectively. The other three colored curves show the HCN cooling rate for the corresponding HCN profiles. Right panel - HCN mixing ratios profiles. The black and purple curves make use of the thermal profile from this work. Due to the significantly cold temperatures above ∼1300 km, HCN is limited by saturation throughout the atmosphere, except in a limited region at 1210-1270 km for an assumed $q_{\rm HCN} = 10^{-7}$. The blue curve shows the hypothetical case of a uniform (i.e. non-limited by saturation) 5×10^{-5} uniform HCN mixing ratio.

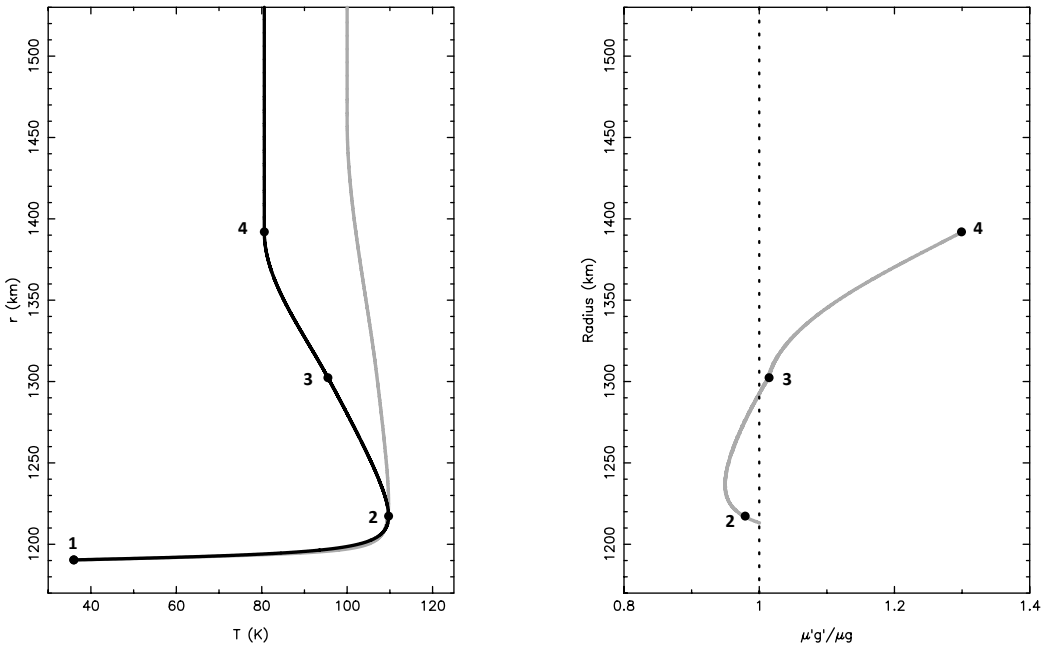

Fig. 12.— Left panel - Solid line: our best temperature profile (see Fig. 13). Gray line: an example of a prescribed profile with milder mesospheric thermal gradient, here a 10 K drop between the stratopause and the mesopause. Right panel - The ratio $\mu' g'/\mu g$, as defined by Eq. 2, corresponding to the gray, prescribed profile of the left panel. The points numbered 2, 3 and 4 correspond respectively to the stratopause, the inflexion point and the mesopause (see also Fig. 13 and text for details).

A. Synthetic light curves

A.1. Parametrized temperature profile

We define a parametric model for Pluto's atmosphere temperature profile, $T(r)$, where r is the radius, i.e. the distance to Pluto's center. The model must be detailed enough to capture the main features revealed by the inversions (Figs. 10 and 13), but still simple enough to allow an easy and meaningful control of $T(r)$ and an assessment of the error bars associated with each parameter. The features we want to describe are: (i) a thin stratosphere just above the surface, with a strong increase of temperature with altitude, (ii) an "elbow" where the temperature reaches its maximum, marking the stratopause, (iii) an intermediate region with a mild negative gradient, and finally (iv) an isothermal upper branch.

These features define three regions, bounded by four points 1,...4 at prescribed radii $r_1, ...r_4$, see Fig. 13. More precisely, the profile $T(r)$ is generated as follows:

$$\begin{cases} c1 \cdot r + c2 \cdot T(r) + c3 \cdot rT(r) + c4 \cdot r^2 + c5 \cdot T^2(r) = 1 & \text{for} \quad r_1 \leq r \leq r_3 \quad \text{(hyperbolic branch)} \\ T(r) = c6 + c7 \cdot r + c8 \cdot r^2 + c9 \cdot r^3 & \text{for} \quad r_3 \leq r \leq r_4 \quad \text{(polynomial branch)} \\ T(r) = T_{\rm iso} & \text{for} \quad r_4 \leq r \quad \text{(straight line)} \end{cases} \tag{A1}$$

Note that r_2 does not appear in the equations above, and is defined as the radius where the temperature reaches its maximum (Fig. 13). The functional forms chosen here (hyperbolic, polynomial and straight lines) are *not* based on physical grounds, but rather, are empirical and simple formulae that satisfactorily fits the observed profiles (Fig. 8).

The parameters $c1, ...c9$ are determined to ensure that $T(r)$ is continuous both in temperature and its derivative, dT/dr, at points 1, 3 and 4. Those conditions provide algebraic systems that are solved by a classical Gauss-Jordan method (Press et al. 1992).

In practice: (1) we fix the temperature $T_1 = T(r_1)$ at the bottom of the profile, together with its gradient $(dT/dr)_1$. (2) We fix the value of the maximum of temperature $T_2 = T(r_2)$ at r_2 and the temperature $T_3 = T(r_3)$ at the inflexion point 3. We thus have three boundary conditions for T: T_1, T_2, T_3 at r_1, r_2 and r_3, respectively, and two boundary conditions for dT/dr: $(dT/dr)(r_1) = (dT/dr)_1$ and $(dT/dr)(r_2) = 0$, which fixes the five coefficients $c1, ...c5$. Note in passing that the values of $c1, ...c5$ then impose the temperature gradient $(dT/dr)_3$ at r_3; (3) We fix the temperature $T_{\rm iso}$ at r_4, the point where the isothermal branch is reached. This provides two boundary conditions in T: T_3 and $T_{\rm iso}$ at r_3 and r_4, respectively, plus two boundary conditions for dT/dr: $(dT/dr)_3$ at r_3 and $(dT/dr)(r_4) = 0$, thus fixing the remaining four coefficients $c6...c9$.

The locations of points 1, 2, 3 and 4 in the space (T, r) are chosen to best fit the observed profiles, see the main text for details. Once $T(r)$ is defined, the gas number density profile $n(r)$ is obtained by integrating the first order differential equation:

$$\frac{1}{n} \cdot \frac{dn}{dr} = -\left[\frac{\mu g(r)}{kT} + \frac{1}{T} \cdot \frac{dT}{dr}\right], \tag{A2}$$

derived from the equation of state for an ideal gas, and the hydrostatic equation. Here,

$$g(r) = \frac{GM}{r^2} \tag{A3}$$

Table 3: Parameters of the two occultations

	18 July 2012	04 May 2013
Star coordinates[1]	α= 18h 32m 14.6720s	α= 18h 47m 52.5322s
	δ= -19d 24' 19.295"	δ= -19d 41' 24.3738"
Ephemeris	DE413/PLU022	DE413/PLU031
Pluto geocentric distance	4.68244×10^9 km (at 04:13 UT)	4.76882×10^9 km (at 08:23 UT)
Sub-observer and sub-solar latitudes[2]	B= +47.10d, B'= +47.54d	B= +49.95d, B'= +48.64d
Pluto's north pole position angle[2]	P= -56.88d	P= -52.91d
Shadow velocity	$\approx$ 23.0 km s^{-1}	$\approx$ 10.6 km s^{-1}
Magnitudes[3]	V= 14.7, R=13.7, K= 10.9	V= 14.1, R=14.0, K= 12.4

[1]J2000, UCAC2 system.
[2]Assuming the Pluto's north pole position (J2000) of Tholen et al. (2008): $\alpha_{\rm p}$= 08h 52m 12.94s, $\delta_{\rm p}$= -06d 10' 04.8"
[3]From NOMAD catalog (Zacharias et al. 2004)

Table 4: Pluto atmospheric model

Physical parameters		
Pluto's mass[1]	$GM = 8.703 \times 10^{11}$ m^3 sec^{-2}	
Nitrogen molecular mass[2]	$\mu = 4.652 \times 10^{-26}$ kg	
Nitrogen molecular refractivity[3]	$K = 1.091 \times 10^{-23} + (6.282 \times 10^{-26}/\lambda^2_{\mu\rm m})$ cm^3 molecule^{-1}	
Boltzmann constant	$k = 1.380626 \times 10^{-23}$ J K^{-1}	
The nine free parameters of the best temperature profile[4]		
r_1, T_1, $dT/dr(r_1)$	$1,190.4 \pm 1$ km, 36 K, 16.9 K km^{-1}	
r_2, T_2	1,217.3 km, 109.7 K	
r_3, T_3	1,302.4 km, 95.5 K (implying $dT/dr(r_3) = -0.206$ K km^{-1})	
r_4, T_4	1,392.0 km, 80.6 K	
The three free parameters particular to each event[5]		
	18 July 2012	04 May 2013
Pressure at $r = 1,275$ km, $p_{1,275}$	2.16 ± 0.02 μbar	2.30 ± 0.01 μbar
Time of closest geocentric approach	04:13:37.24±0.07 UT	08:22:27.11±0.09 UT
Distance of closest geocentric approach[6]	-404.6 ± 2.7 km	-723.5 ± 2.7 km

[1]Tholen et al. (2008). [2]Assumed to be the only constituent in the ray tracing code, see text. [3]Washburn (1930). For both NACO observations of 2012 and 2103, H band ($\lambda = 1.6$ μm) was used. [4]Or equivalently, the nine coefficients $c1, ...c9$, see text and Fig. 13 for the definition of the various quantities given here. [5]So that there are twelve free parameters for each date. [6]Distance of Pluto's center to the star at closest approach, projected in the sky plane, as seen from the geocenter. A negative value means that Pluto's center went south of the star in the sky plane.

is the acceleration of gravity, assuming a spherical, homogeneous planet. The values of μ (Table 4) corresponds to molecular nitrogen, assumed to be the unique gas present in the atmosphere. Also listed in Table 4 are the Boltzmann constant k and Pluto's mass parameter GM.

A boundary condition is required to integrate Eq. A2, e.g. the pressure $p_{1,275}$ at $r = 1,275$ km, which fixes the needed boundary condition $n_{1,275} = P_{1,275}/kT_{1,275}$. Finally, the refractivity $\nu(r)$ of the gas (index of refraction minus unity) is given by

$$\nu(r) = K \cdot n(r), \tag{A4}$$

where the molecular refracticity is given in Table 3, assuming again pure molecular nitrogen. Once $\nu(r)$ is obtained, we can derive the vertical refractivity gradient $d\nu/dr$ that is used in the ray tracing code, see below.

The inversions proceed the other way around: the light-curves provide $d\nu/dr(r)$ through an abelian integral (Vapillon et al. 1973), then $\nu(r)$, from which $n(r)$ is derived (Eq. A4), followed by the temperature profile, once a boundary condition is given for T (Eq. A2)

A.2. Ray tracing

For small values of ν (as it is the case here) and under spherical symmetry assumption, a stellar ray is deviated by $d\omega = (\partial\nu/\partial r) \cdot ds$ (Snell-Descartes law) as it moves along an elementay path ds. In principle, a ray tracing code should account for the curvature of the stellar ray as it is refracted in the atmosphere. In practice, however, it is enough to assume that the ray has a rectilinear trajectory in the entire atmosphere. In fact, the maximum total deviation ω suffered by the ray is very small for ground-based occultations, more precisely of the order of Pluto's apparent angular radius, $\sim$0.05 arcsec, so that $\omega <\sim 3 \times 10^{-7}$ rad. Most of that deviation occurs in the deepest scale height H traversed at radius r, which represents a traveled length of $l \sim \sqrt{2\pi r H}$ (Baum and Code 1953). Taking typical values of $r \sim 1,200$ km and $H <\sim 50$ km, we get $l <\sim 600$ km, i.e. a deviation inside the atmosphere of $\sim \omega \cdot l < 0.2$ meters, which is negligible compared to the scales probed by ground-based stellar occultations.

The numerical integration of Eq. A2, using a second order scheme, provides $n(r_i)$ at discreet layers of radii r_i, from which the refractivity ν_i and its gradient $(d\nu/dr)(r_i)$ are calculated. The total deviation along the straight line s is then:

$$\omega = \sum_i \Delta\omega_i = \sum_i (d\nu/dr)(r_i) \cdot \Delta s_i, \tag{A5}$$

where Δs_i is the path along s traveled inside the layer i. Then, for a closest approach r of a ray to Pluto's center, the corresponding distance z to the shadow center upon arrival on Earth is

$$z = r + \omega(r) \cdot D, \tag{A6}$$

where D is Pluto's geocentric distance. The observed stellar flux is then

$$\Phi(z) = f \frac{dr}{dz} = \frac{1}{1 + D d\omega/dr}, \tag{A7}$$

where $f = r/z$ is the focusing factor due to the (assumed circular) limb curvature, see Sicardy et al. (1999).

The thickness Δr_i of the individual refracting layers has been adjusted to 30 meters to minimize numerical noise, while keeping computing times reasonably low. Similarly, the sampling for r (the closest distance

of the rays to Pluto's center) has been adjusted so that adjacent rays arrive at separation $\Delta z \approx 1$ km in the shadow plane.

Once the table $(r, z, \Phi(z))$ has been completed, the synthetic flux at a given site and given moment (corresponding to a distance $z_{\rm obs}$ of the observer to the shadow center) is calculated by interpolation. If several stellar images are present, all the fluxes are summed. In the particular case of a spherically symmetric atmosphere, and for a given distance $z_{\rm obs}$, there is a primary image corresponding to $z = z_{\rm obs}$, and a secondary image corresponding to $z = -z_{\rm obs}$.

The lowest radius r_1 considered in the model (1,190.4 km, see Table 4 and Fig. 13) is adjusted so that the corresponding flux received in the shadow plane is $\sim 10^{-3}$ of the unocculted stellar flux, negligible compared to the noise level of the best light-curves. The upper limit for the atmosphere has been fixed to a radius of about 2,300 km. This corresponds to a pressure level of about 0.05 nbar, at which point the stellar drop is several orders of magnitudes less than the noise in our best light-curves.

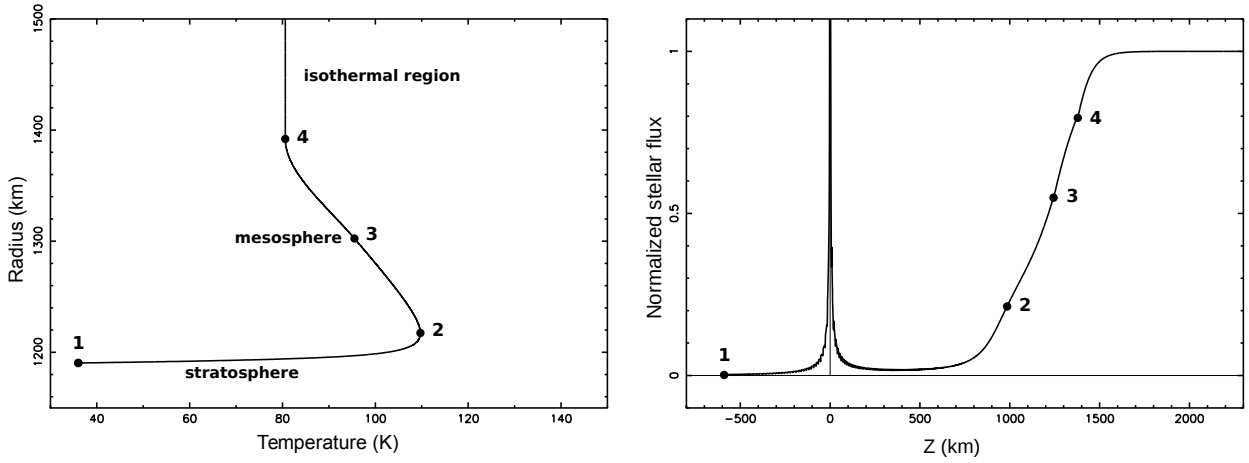

Fig. 13.— Left - The temperature profile $T(r)$ that best fits our 2012 and 2013 light-curves, see Figs. 3 and 4. The parameters used to generate this profile are given in Table 4. Total thickness of the atmosphere: 1100 km, vertical sampling of the model: 0.03 km. Right - The corresponding synthetic flux in the shadow plane for the 18 July 2012 occultation. Here, z is the distance to the shadow center, with the four points corresponding to those of the left panel.

The profile that best fits our light-curves is shown in Fig. 13. The trajectories of the primary and secondary stellar images as seen from VLT on 18 July 2012 are displayed in Fig. 2.

The best fits to the observed light-curves are shown in Figs. 3 and 4. Their quality is assessed through the so-called χ^2 per degree of freedom:

$$\chi^2_{\rm dof} = \frac{\chi^2}{N-M} = \frac{1}{N-M} \sum_{i=1}^{N} \left(\frac{\Phi_{\rm obs,i} - \Phi_{\rm syn,i}}{\sigma_i} \right)^2 , \qquad \text{(A8)}$$

where $\Phi_{\rm obs,i}$ (resp. $\Phi_{\rm syn,i}$) is the observed (resp. synthetic) stellar flux of the $i^{\rm th}$ data point, σ_i is its associated standard deviation, where the summation is extended to the N data points from all the light-curves used in

the fit, and M is the number of free parameters of the model. As we have nine coefficients $c_1, ...c_9$ to define $T(r)$ (Eq. A1), a boundary condition $p_{1,275}$ and two quantities to define Pluto's center, $M = 12$.

B. Noise propagation

B.1. Photometric noise

Here we estimate the effect of photometric noise in an occultation light-curve on the retrieved density, temperature and temperature gradient profiles. We denote δ the fluctuation of a given quantity, and $\sigma = \sqrt{\overline{\delta^2}}$ its standard deviation, where the bar denotes average values. For estimation purposes, it is enough to assume here (but not in the ray-tracing or inversion procedures) that the atmosphere has locally a constant density scale height H that is small compared to the planet radius. The stellar flux is then given by the Baum and Code (BC) equation (Baum and Code 1953):

$$\frac{1}{\Phi} - 2 + \log\left(\frac{1}{\Phi} - 1\right) = -\frac{z - z_{1/2}}{H}, \tag{B1}$$

where $z_{1/2}$ is the position in the shadow plane at which $\Phi = 1/2$ (half-light level).

We focus on the top of the profiles, corresponding to $\Phi \sim 1$, so that Eq. B1 becomes $\Phi(z) \sim 1 - \exp[-(z - z_{1/2})/H]$. Morever, for $\Phi \sim 1$, the stellar ray deviation ω is small, and we can equate r and z, see Eqs. A6 and A7, where $f \sim 1$. In the BC approximation, we have $\omega \sim -\nu\sqrt{2\pi r/H}$, where ν is the refractivity at r. As the atmosphere density profile is basically exponential, $d\omega/dr \sim -\omega/H = \nu\sqrt{2\pi r/H^3}$, so that Eq. A7 can be used to estimate the expected refractivity corresponding to a stellar flux Φ, namely $\nu \sim (1 - \Phi)\sqrt{H^3/2\pi r D^2}$

We denote ν_0 and r_0 the refractivity and corresponding radius where the stellar drop is equal to the standard deviation of the flux, σ_Φ, i.e.

$$\nu_0 \sim \sigma_\Phi \sqrt{\frac{H^3}{2\pi r D^2}}. \tag{B2}$$

Thus, r_0 is the radius where the stellar drop starts to be barely significant, given the photometric noise. At the upper part of the profiles, we have $H \sim 60$ km. The 18 July 2012 NACO lightcurve has a photometric standard deviation of $\sigma_\Phi = 0.011$. Using the value of D given in Table 3, we obtain $\nu_0 \sim 1.3 \times 10^{-11}$. Assuming a pure N_2 atmosphere, we obtained the corresponding molecular density $n_0 = \nu_0/K \sim 6 \times 10^{12}$ cm^{-3}, which is reached at radius

$$r_0 \sim 1,565 \text{ km}.$$

For $\Phi \sim 1$ (and $f \sim 1$), and using the results above, Eq. A7 provides $\Phi \sim 1 - D d\omega/dr = 1 + \sqrt{2\pi r D^2/H}(d\nu/dr)$. For a *noise-free* light-curve, we expect $\Phi = 1 - \sigma_\Phi \exp[-(r - r_0)/H]$. In reality, Φ is affected by fluctuations δ_Φ, so that the retrieved refractivity gradient is in fact: $d\nu/dr = (\nu_0/H) \cdot [-\exp[-(r - r_0)/H] + \delta_\Phi/\sigma]$. Consequenly, the standard deviation associated with each point of the $(d\nu/dr)(r)$ profile (and restricting ourselves to the top of the profile) is:

$$\sigma_{d\nu/dr} \sim \frac{\nu_0}{H}$$

The profile $(d\nu/dr)(r)$ is the primary result derived from the light-curve, and from which all the other profiles are deduced. Once $d\nu/dr$ is known, we have to estimate $\nu(r) = \nu_1 + \int_{r_1}^{r}(d\nu/dr)dr$, where

$(r_1, \nu_1 = \nu(r_1))$ is a boundary condition. The integration is performed numerically by taking $\nu(r) = \nu(r_1) + \sum_{i=1}^{N} (d\nu/dr)(r_i) \cdot \Delta r$, where Δr is the spatial sampling of the data (i.e. Δr = the star velocity perpendicular to the limb multiplied by the exposure time). Thus, $r_i = r_1 + (i-1)\Delta r$ and $N = |r - r_1|/\Delta r$. Adding the variances associated with individual $(d\nu/dr)(r_i)$'s, we obtain:

$$\sigma_\nu \sim \sqrt{\frac{|r - r_1|}{H} \frac{\Delta r}{H}} \nu_0 \sim \sqrt{\frac{\Delta r}{H}} \nu_0,$$

where the second approximation stems from the fact that r_1 is chosen close to r_0 and that we are considering here the few top scale heights of the profiles, so that $|r - r_1|/H \sim \mathcal{O}(1)$. Note that $\sigma_\nu = 0$ for $r = r_1$. This is because (r_1, ν_1) is an arbitrary boundary condition, and such, has no associated error bars.

From $n = \nu/K$, we obtain the standard deviation associated with the density gradient and the density itself: $\sigma_{dn/dr} = \sigma_{d\nu/dr}/K$ and $\sigma_n = \sigma_\nu/K$. Moreover, from Eq. A2, and assuming an isothermal upper atmosphere, we obtain $\delta_{dT/dr} = -(T/n)\delta_{dn/dr}$, so that $\sigma_{dT/dr} = (T/n)\sigma_{dn/dr}$. Finally, the temperature profile is obtained from the numerical integration of $T(r) = T_2 + \int_{r_2}^{r} (dT/dr)dr$, where $(r_2, T_2 = T(r_2))$ is an arbitrary boundary condition. Using the same line of reasoning as for $n(r)$, we obtain σ_T by adding the variances $\sigma^2_{dT/dr}$ of all the points $i = 1...N$ involved in the integration, where now $N = |r - r_2|/\Delta r$. Combining the results above, we obtain the following standard deviations for $n(r)$, $T(r)$ and $(dT/dr)(r)$:

$$\sigma_n \sim \sqrt{\frac{\Delta r}{H}} n_0, \quad \sigma_T \sim T\sqrt{\frac{\Delta r}{2H}} \sqrt{\left| e^{2(r-r_2)/H} - 1 \right|} e^{(r_2 - r_0)/H}, \quad \sigma_{dT/dr} \sim \frac{T}{H} e^{(r-r_0)/H} \tag{B3}$$

Fig. 8 shows the $\pm 1\sigma$ envelopes at the upper parts of the various profiles. We take here $r_2 = 1,390$ km, the radius at which we fix a prescribed temperature $T_2 \sim 81$ K. Note again that $\sigma_T = 0$ at $r = r_2$, as (r_2, T_2) is an arbitrary boundary condition. Finally, the envelopes $\pm 1\sigma$ are plotted only down to the half-light level ($r \sim 1,290$ km), as the estimations made here apply only for the upper part of the light-curve. In any case, below that level, the uncertainties in the profiles are dominated by the uncertainty on the background Pluto + Charon contribution, see below.

B.2. Effect of the Pluto and Charon flux contributions

The stellar flux reaches its minimum value in the shadow at typically $z_{\min} \sim (z_{1/2})/2$, i.e. half-way between the half-light level and the shadow center, where the central flash occurs (Fig. 13). At the minimum, we have from Eq. B1: $\Phi_{\min} \sim H/(z_{1/2} - z_{\min}) \sim 2H/z_{1/2}$. Eq. A2 then provides

$$H = \left| \frac{n}{dn/dr} \right| = \frac{T}{(\mu g/k) + (dT/dr)} \sim \frac{z_{1/2}}{2} \Phi_{\min}. \tag{B4}$$

At the bottom of the temperature profile (stratosphere), $\mu g/k$ and dT/dr are of same order of magnitude. Consequently, increasing the value of the Pluto + Charon contribution to the light-curve decreases the value of Φ (Fig. 7), thus increasing the retrieved gradient dT/dr. This is illustrated in Fig. 9.

B.3. Effect of initial conditions

Once the density profile $n(r)$ is derived from the inversion, Eq. A2 yields the temperature profile $T(r)$, provided a boundary condition $T_b = T(r_b)$ is fixed at an arbitrary level r_b. Let us consider two possible

solutions $T(r)$ and $(T+\Delta T)(r)$ that differ by $\Delta T(r_b)$ at r_b, then expanding Eq. A2 to first order in $(\Delta T/T)(r)$, we obtain:

$$\frac{d}{dr}\left(\frac{\Delta T}{T}\right) \sim \frac{1}{H}\left(\frac{\Delta T}{T}\right),$$

where we have approximated $H \sim kT/\mu g$. Thus, as r increases, the relative difference $\Delta T/T$ diverge exponentially as:

$$\left(\frac{\Delta T}{T}\right)(r) \sim \left(\frac{\Delta T}{T}\right)(r_b) \cdot e^{(r-r_b)/H} \tag{B5}$$

This exponential divergence should not been confused with the one that is provided by Eq. B3 for σ_T. The latter tends to zero as the noise tends to zero, while the former is inherent to the nature of Eq. A2.